

Task 4: Oxide Characterization

One of the main goals of this project is to discern the microstructural differences of oxides formed in different model alloys under the same conditions. The idea is to relate these microstructure differences to the corrosion kinetics and to the stability of the oxide. To that purpose we performed a systematic characterization of the oxides using a variety of experimental techniques. These observations are summarized in this section, and illustrated by the relevant data.

As mentioned in sections 2 and 3, the model alloys in this work were tested under three different conditions: (i) in water at 360 °C, (ii) in steam at 500 °C (1500 psi) and (iii) in supercritical water at 500 °C (3500 psi). The general procedure was to archive samples at different stages in the corrosion process to be examined. For each model alloy, there were 8 coupons tested at each corrosion condition, and coupons were taken out at set intervals to typify particular stages in the corrosion process. For example, Figure 4.1 shows the weight gain versus exposure time for Zircaloy-4 samples tested in 360°C water. As mentioned in section 2, there is good reproducibility from sample to sample. The red dots indicate where samples were archived. In this case, samples were taken just before (28 and 150 days) and after (180 and 240 days) the oxide kinetic transition, after the second transition at 353 days and so on. The equivalent data for all the alloys in this study is in Appendix A.

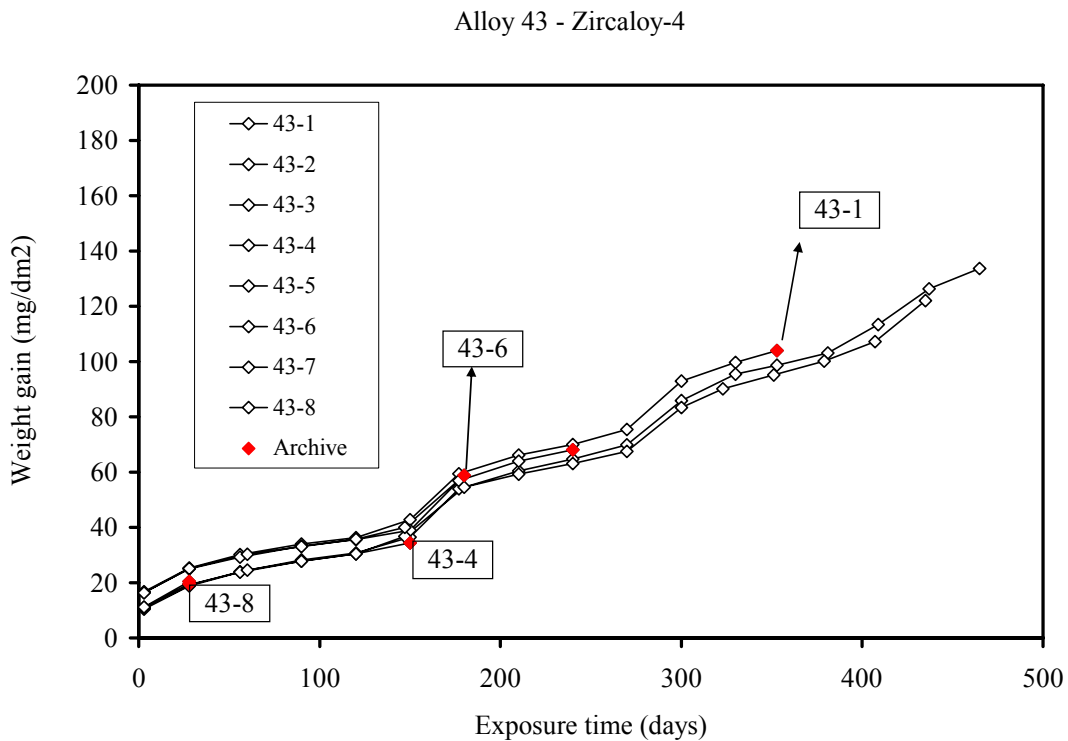


Figure 4.1: Oxide weight gain *versus* exposure time for Zircaloy-4 in 360°C water highlighting the samples archived (red points) for oxide characterization.

The main technique used to characterize the oxide layers was synchrotron radiation diffraction and fluorescence, both using cross sectional microbeam and using frontal bulk diffraction. Basic oxide cross-sectional examinations were performed using optical and SEM. Additional characterization was performed using TEM. We summarize these observations in this section.

4.1 Optical examination and SEM examination

General aspect of oxide surfaces

As shown in Figure 2.6 which shows corrosion coupons tested in water at 360°C water (reproduced as Figure 4.2), the clearest difference between the general aspect of oxides formed during protective and non-protective behavior is their color. Generally, protective oxides tend to be black, adherent and shiny, while non-protective oxides tend to be whitish, matt and flaky. At the two extremes, the protective oxides (Zr_{0.4}Fe_{0.2}Cr (H), 14-8 and 14-9) are black and shiny while the non-protective ones are whitish and the oxide tends to flake off upon handling (crystal bar Zr, 42-2 and 42-3). The earlier stages of non-protectiveness in crystal bar Zr are whitish and irregular (samples 42-12 and 42-15), while localized corrosion is seen in sample 34. The samples 21 and 33 show intermediate behavior in the form of grayish or green oxides, indicating somewhat less protective oxides.

Oxides that are semi-protective (i.e. undergo kinetic transition but recover protective character later) show an in-between, grayish appearance. In addition, a few samples showed oxide spallation at the edges and were disregarded in the final analysis (they considered to have fabrication artifacts). It should also be noted that one of the alloys (ZrCr) showed a protective oxide that was light green in color. Finally as illustrated in section 3, a few samples underwent localized corrosion (nodular corrosion) during high temperature testing.

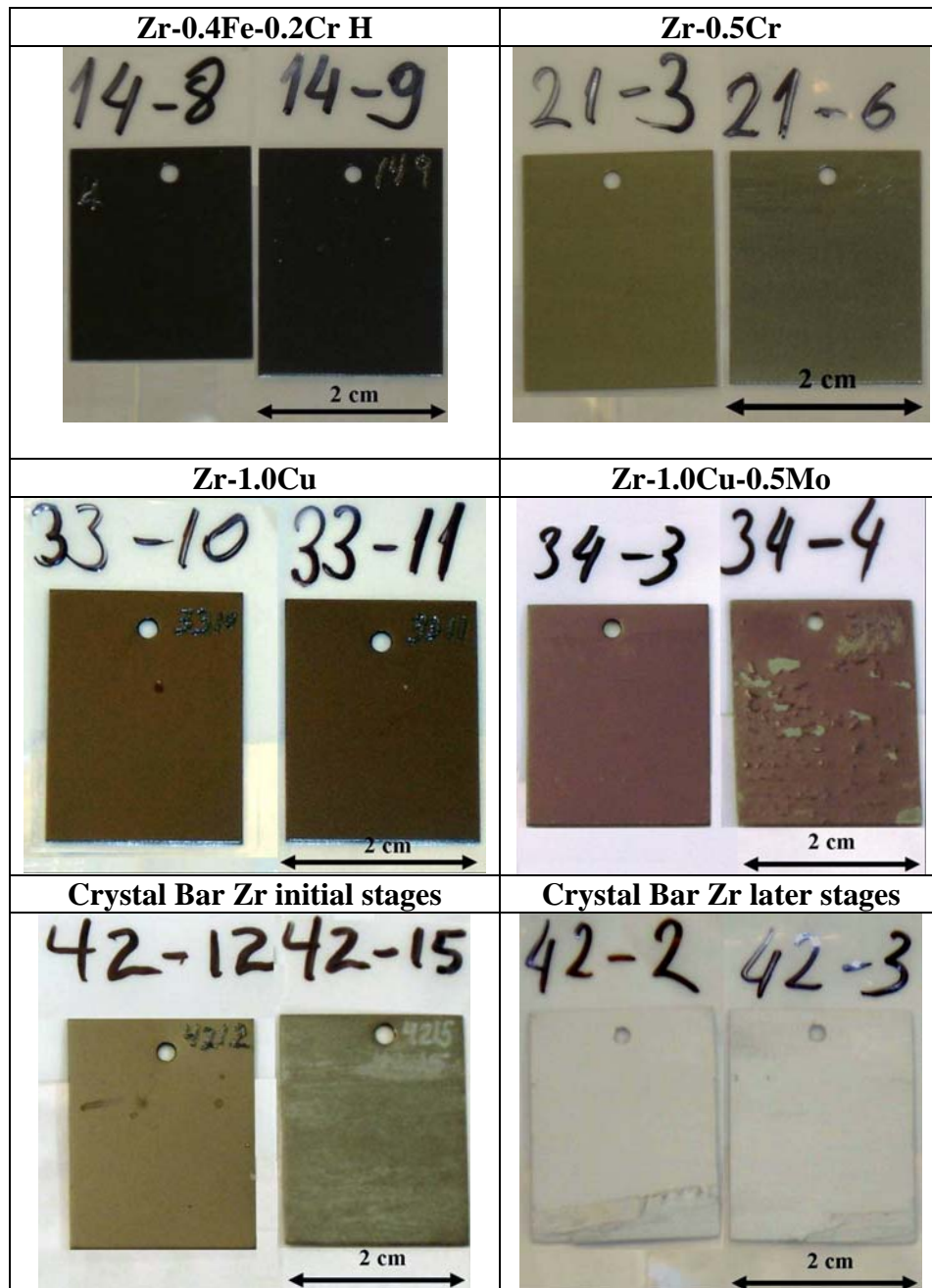


Figure 4.2: Visual appearance of oxide coupon samples formed on various model alloys after corrosion in water at 360°C.

Optical and SEM examinations of Cross sectional Oxides

Metallographic cross sections were prepared to examine the oxide metal interface for oxides formed in model alloys. In general, the non-protective oxides were significantly more cracked than the protective oxides, and their oxide metal interfaces were more irregular. Stable protective oxide growth was associated with an even, homogeneous uncracked oxide. The extreme example of a non-protective oxide is given by the oxides

formed in pure Zr (both sponge and crystal bar). Figure 4.3 shows an oxide formed on sponge Zr before (a) and after (b) the breakaway. The oxide formed before the breakaway is protective, uncracked and homogeneous while the oxide formed after the transition grows unevenly, with oxide “fingers” going into the metal and large scale cracking occurring.

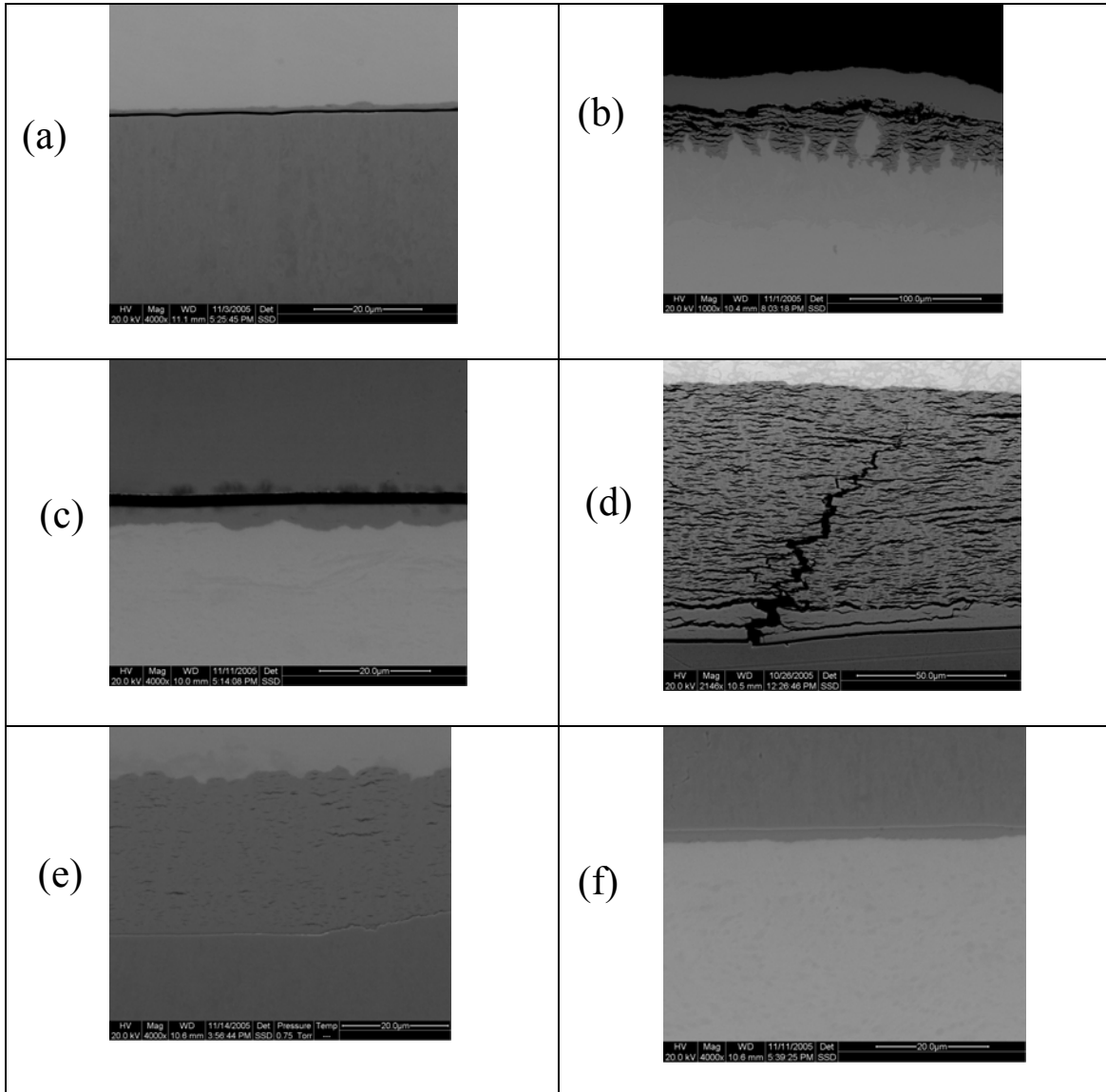


Figure 4.3: Cross sectional scanning electron micrographs of oxides formed on various Zr alloys during corrosion in 360°C water. (a) sponge Zr, seven days exposure (pre-breakaway), (b) crystal bar Zr, 3 days exposure (breakaway), (c) Zr1.0Cu0.5Mo, 150 days exposure (pre-breakaway), (d) Zr1.0Cu0.5Mo, 240 days exposure (breakaway), (e) Zr0.5Cr 146 day exposure after breakaway and (f) Zr0.4Fe0.2Cr (H) 180 days (no breakaway seen).

Figure 4.3 (c) and (d) show alloy Zr1.0Cu0.5Mo which behaved in a protective manner and then lost protectiveness. Large scale cracking is seen after the oxide becomes non-

protective, however the oxide-metal interface is more homogeneous than in 4.3 (b). Finally 4.3 (e) shows the layers of cracks formed on Zircaloy-4 upon several kinetic transitions and Figure 4.3 (f) shows alloy $Zr_{0.4}Fe_{0.2}Cr(H)$ which did not lose protectiveness for the full duration of the test.

As can be seen in Figure 4.3, in general, the oxide metal interface was less wavy and more homogeneous in protective oxides. This suggests that the mechanism of the oxide instability might be related to lateral variations in the growth rate of the oxide. Since the instabilities are very pronounced in pure Zr but diminish with the presence of a small amount of alloying elements, one natural hypothesis is that the alloying elements provide additional conductivity to the oxide layer by the presence of intermetallic precipitates. More importantly, the presence of such precipitates would make oxide conductivity be more laterally homogeneous. In the absence of such precipitates the oxide conductivity would be lower and the transport of electrons that helps close the circuit of the corrosion process will be more difficult. The remnant conductivity will then vary with whatever impurities exist in the oxide, and short circuits could exist that would cause the local corrosion rate to increase.

Zircaloy-4 exhibited marked kinetic transitions as seen in Figure 4.1, the traces of which could be seen in the form of a layer of cracks spaced parallel to the oxide metal interface, which appear with the spacing correspondent to the thickness at which transitions are observed, as seen in Figure 4.4. Other Sn containing alloys also exhibited transitions such that it may be possible to associate marked oxide kinetic transitions with the presence of Sn.

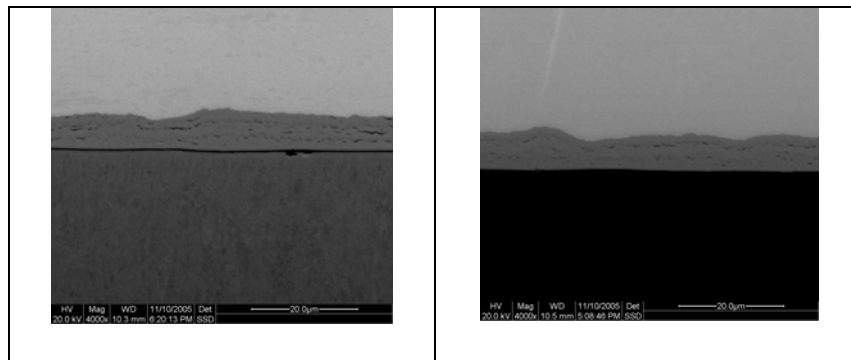


Figure 4.4: (a) Zircaloy-4 after 353 days exposure in 360°C water (two or three transitions) and (b) $Zr_{0.2}Nb$ after 60 days in 360°C water.

Similar features were observed in the oxides formed during high temperature testing. Figure 4.5 shows a sequence of cross sectional images of the oxides formed in the best performing model alloys during 500°C supercritical water testing. It is clear that these protective oxides are homogeneous and that the interfaces are smooth. Another feature that can be observed in these pictures is the diffusion layer seen just ahead of the oxide metal interface. This layer is similar to the layer observed during corrosion of zirconium alloys at lower temperature and consists of oxygen dissolved into the Zr matrix, to near the solubility level (about 30 at. %) and forming a sub-oxide phase [1]. The difference

here is that the diffusion (or sub-oxide) layers observed at lower temperature were 0.1 to 0.5 microns thick, whereas these layers are 5 to 6 microns thick. In this case the layers are thick enough that the weight gain has to be corrected for the fact that not all oxygen that goes into the metal forms Zr dioxide [2].

This observation, coupled with others regarding oxide phases present and oxide texture, suggests that the corrosion protection mechanisms are similar at 360°C and at 500°C although the kinetics are faster at the higher temperature.

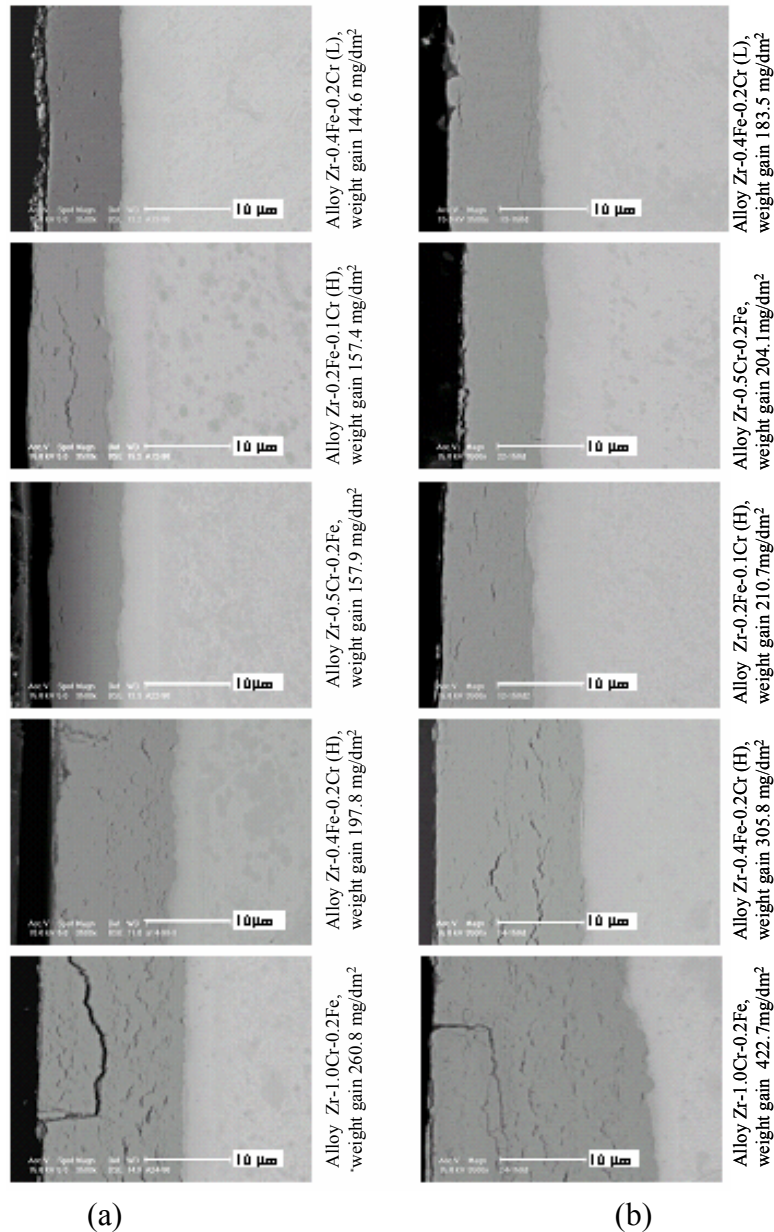


Figure 4.5. Cross section images of the coupons and their weight gains following (a) 90 days and (b) 150 days of exposure in deaerated SCW at 500°C.

4.2. Overall oxide texture determination using synchrotron radiation diffraction

The oxides that grow on Zr alloys are highly textured. This is because as the oxide grows, stresses can accumulate that can be minimized by proper oxide orientation [3]. In addition there are orientation relationships that cause the oxide to grow with a preferential orientation relative to the base metal.

The experimental procedure is illustrated in Figure 4.6. A 17 keV synchrotron radiation beam was incident on the sample at a glancing angle of 3-4 degrees (4.6a). Diffraction patterns were collected on an image plate, at various values of the sample normal angle (ϕ) by rotating the sample around the normal by 5 degrees from 0 to 200 degrees. The recorded images were integrated along the diffraction rings by 5 degrees sectors, effectively varying along the angle χ (4.6b and d). Integrating along each ring we obtained partial pole figures for the peaks of interest (mostly monoclinic ZrO_2). The pole figure coverage is illustrated in Figure 4.6c, which corresponds to about 0-70 degrees χ and 0-200 degrees ϕ .

In this manner we can *simultaneously* obtain the partial pole figures for the various poles of interest. For the two-theta range we examined, pole figures can be obtained for the following poles: 110_M , 011_M , -111_M , 111_M , 200_M , 020_M , 002_M , -201_M . In the 200_M family of planes the peaks often overlap with each other and with other peaks from metal phases, so care needs to be exercised in the interpretation. Nevertheless, especially for the peaks that stand on their own, pole figures can be obtained for all peaks in the chosen two-theta range, with a single data collection.

This was done for oxides formed on the various alloys. Figure 4.7 shows a set of partial pole figures obtained by the procedure above from an examination of a protective oxide formed on ZIRLO in pure water. Figure 4.8 shows a comparison between the pole figures of three different oxides formed in ZIRLO-protective (4.8a), Zr-0.5Cu-0-.5Mo (semi-protective, 4.8b) and sponge Zr (non-protective 4.8c).

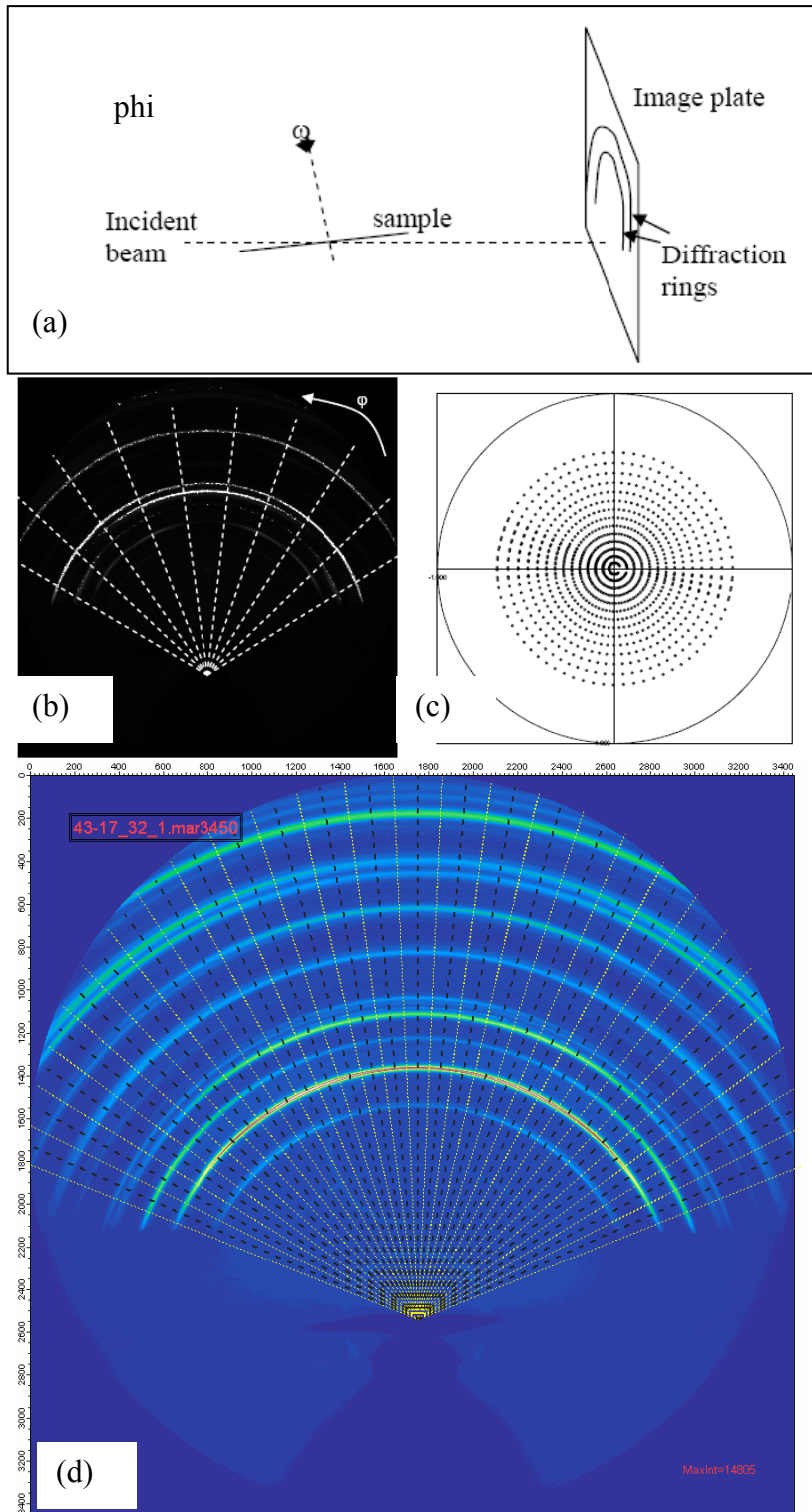


Figure 4.6: (a) Schematic experimental setup (b) integration procedure, (c) pole figure coverage and (d) actual diffraction pattern from Zircaloy-4 sample 43-17, collected in the image plate having the 5° integration sectors superimposed.

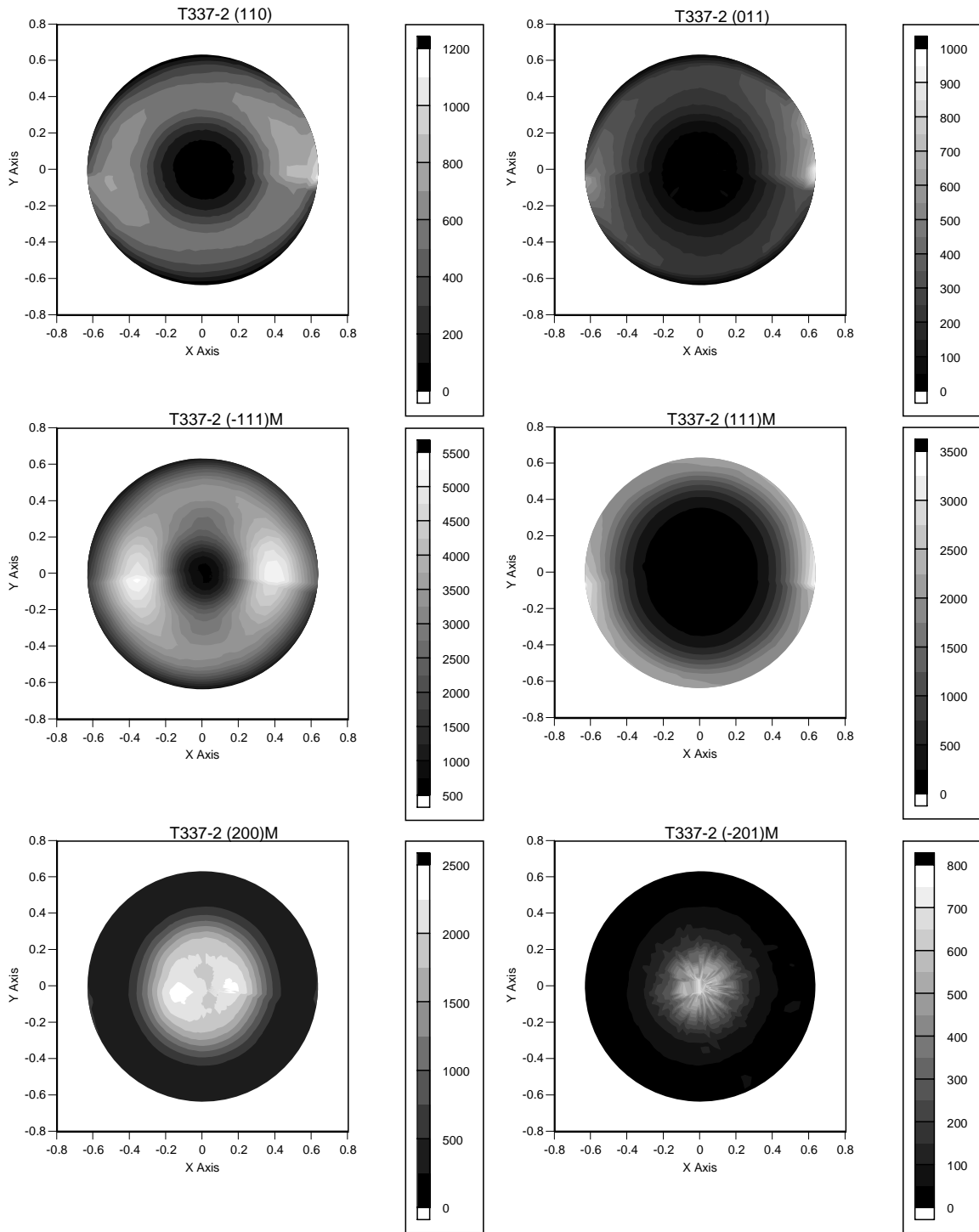


Figure 4.7 Partial pole figures for various monoclinic ZrO_2 poles, as indicated, obtained from an oxide formed on ZIRLO during corrosion testing in 360°C water

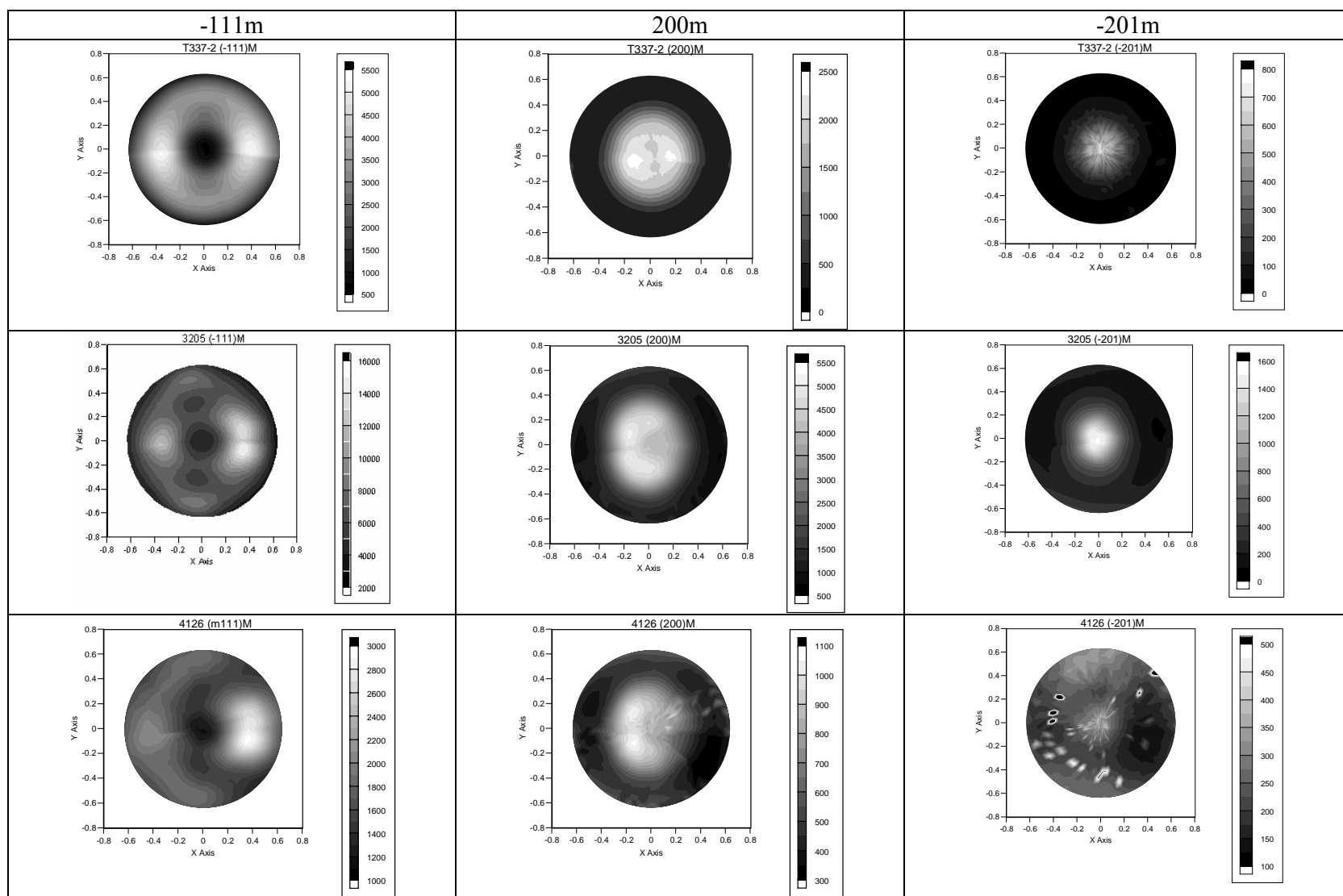


Figure 4.8: Partial pole figures for various monoclinic poles as indicated, for three oxides formed during exposure to 360°C water in (a) ZIRLO (protective oxide) , (b) Zr_{0.5}Cu_{0.5}Mo (semi protective oxide), and (c) sponge Zr (non-protective).

The results show that in many ways the similarities in oxide texture for protective and non-protective oxides are greater than the differences, both at low and at high temperature. By calculating the angle between the maxima of different poles and the normal direction the oxide growth direction has been determined to be between $\bar{2}01_M$ and $\bar{4}01_M$. Previous researchers have shown that the theoretical ideal oxide growth direction (from the point of view of minimizing stresses) is the $\bar{6}01$ monoclinic oxide direction, but that the actual oxides grow in between the $\bar{4}01$ and $\bar{3}01$ directions [4], in agreement with this work.

The degree of oxide orientation in the 200_M direction was measured by calculating the resolved fraction of $[200]_M$ poles along the growth direction of the oxide, (analogously to the Kearns factor in Zr alloys [5]) for various oxides. These values were found to be similar for the various oxides studied (oxides formed on alloys 11, 22, 23, 33, 34, before and after breakaway), so this is not a distinguishing feature of protective and non-protective oxides. For both protective and non-protective oxides, the $\{\bar{1}11\}$ planes show two lobes oriented with their normals (poles) along the transverse x normal plane of the metal, and about 40-45 degrees from the oxide growth direction. The difference is that the $[\bar{1}11]_M$ and $[200]_M$ diffraction lobes exhibit about the same intensity (and are less localized) in the protective oxides and significantly skewed (one lobe stronger than the other) in the non-protective oxides.

This is also true during high temperature corrosion testing. Figure 4.9 shows three partial pole figures obtained using synchrotron radiation diffraction for two oxides formed at high temperature, one protective and one non-protective oxide. The two oxides are formed on Zr0.5Cr in 500°C steam and Zr1.0Cr0.2Fe in supercritical water. The latter forms a protective oxide while the former forms a non-protective oxide.

The figures above show that the oxides form with the growth direction aligned close to $[\bar{2}01]_M$ (and thus close to $\bar{3}01$), as the intensities of the $[\bar{2}01]_M$ pole figure are at a maximum close to the normal direction (i.e. the growth direction). The intensities of the $[\bar{1}11]_M$ poles are mostly aligned in the TN plane, about 40-45 degrees from the normal (more so for the Zr0.5Cr non-protective oxide than for the Zr1.0Cr0.2Fe protective oxide). This results from the previously determined orientation relationship $[200]_M // [0002]_{hcp}$ and $[020]_M // [10\bar{1}0]_{hcp}$ [1].

It was a common observation in the non-protective oxides that one of the $[\bar{1}11]_M$ lobes was systematically stronger than the other. This may indicate that during non-protective oxide growth, the balance between the possible variants of growth that obey the orientation relationship above is perturbed, so that colonies of grains in one orientation dominate. A corresponding imbalance is seen in the $[200]_M$ peak, which in the top left part of Figure 4.9 shows a higher intensity to the left of normal (whereas the $[\bar{1}11]_M$ is right of the normal). In contrast, in the protective oxide, the $[\bar{1}11]_M$ intensities are less concentrated in the TN plane and are more evenly distributed in the circumferential direction. Whether the unequal distribution of intensities between possible $[\bar{1}11]_M$ orientations is a cause or an effect of the oxide lack of protectiveness is open to question.

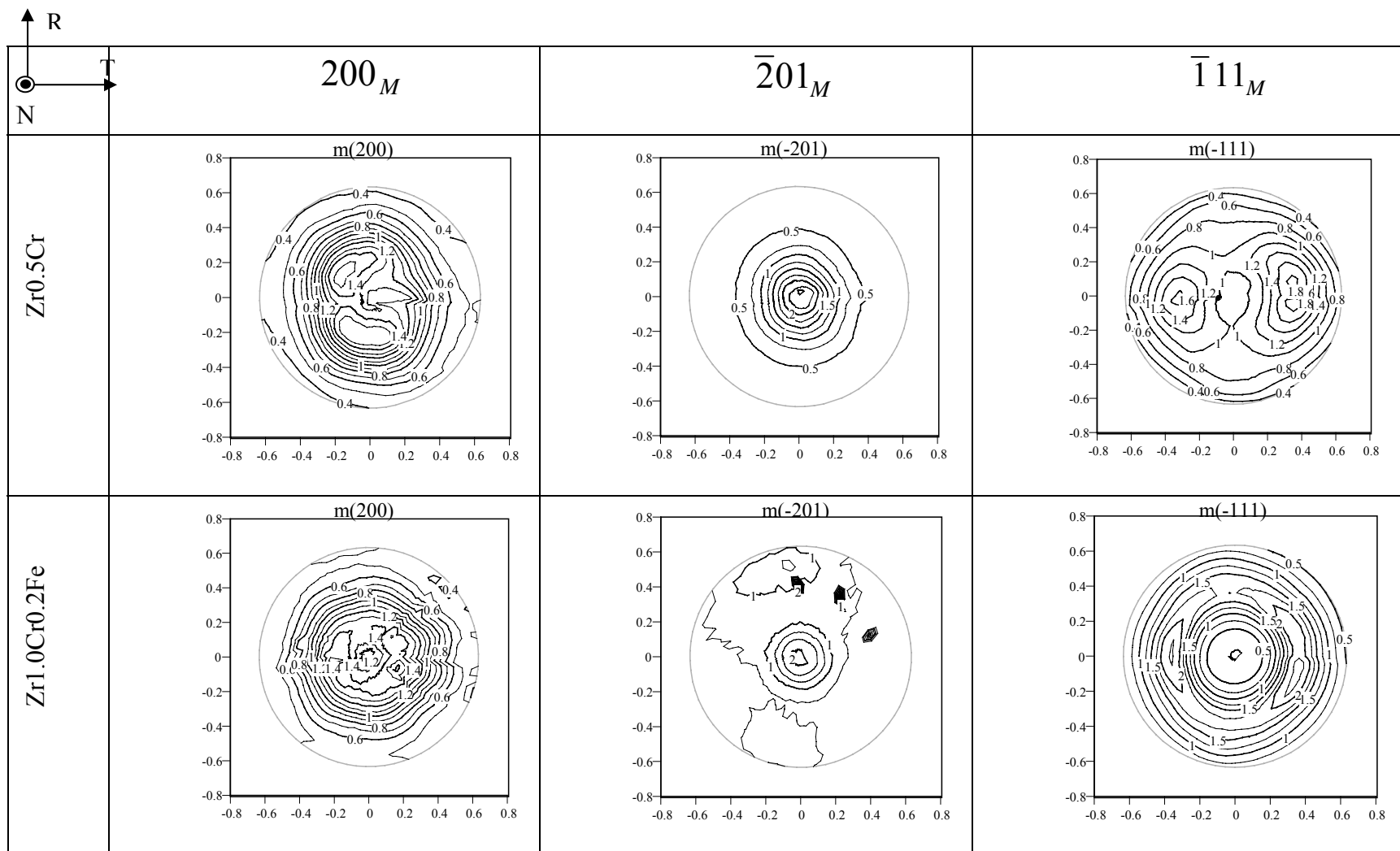


Figure 4.9: Pole Figures for the ZrO₂ monoclinic peaks indicated, and obtained as averaged over the oxide layer, in frontal geometry for two oxides, one non-protective (Zr_{0.5}Cr) and one protective (Zr_{1.0}Fe_{0.2}Cr). These figures are normalized such that the level “1” corresponds to the average intensity.

4.3 Oxide structure studied using microbeam synchrotron radiation diffraction and fluorescence

To study in greater detail the phases formed, grain size, local texture (oxide orientation), and the structure of the oxide-metal interface, we utilized microbeam synchrotron radiation diffraction and fluorescence. This technique has been applied by our group to study the structure of metals and oxides[1, 2, 6-11].

Experiments were performed at the Advanced Photon Source (APS) at Argonne National Laboratory. The experimental setup is shown in Figure 4.10.

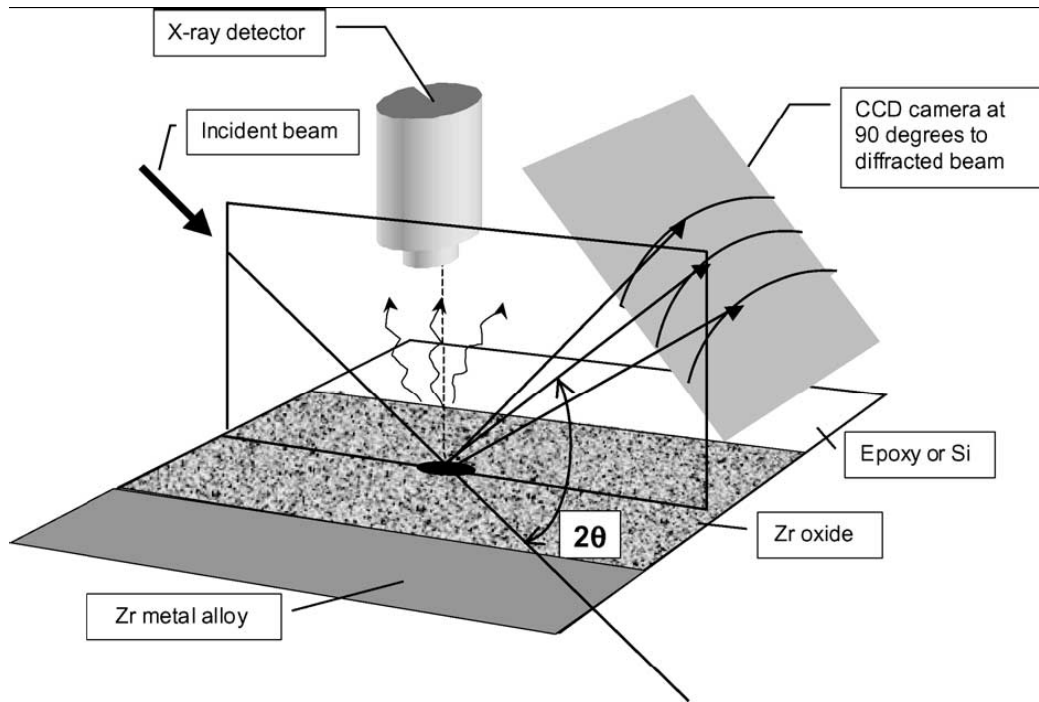


Figure 4.10: Schematic drawing showing the acquisition geometry for microbeam synchrotron radiation diffraction and fluorescence.

The beamline (2ID-D) utilized is equipped with zone plate diffraction gratings that can produce a monochromatic $0.2 \mu\text{m} \times 0.3 \mu\text{m}$ X-ray beam with a photon flux of 5×10^9 photons/s and an X-ray energy band width (dE/E) of 0.01 % [12]. The beam that was used during the experiments was focused to a size of $0.25 \mu\text{m}$ in the vertical direction (normal to the oxide-metal interface) so that it had a $2 \mu\text{m}$ footprint in the horizontal direction (parallel to the oxide-metal interface). The beam energy was 9.5 keV, corresponding to a wavelength of 0.1305 nm. Diffraction and fluorescence data were simultaneously collected from the sample as it was translated across the beam in step sizes ranging from 0.15–0.50 μm . The diffraction data were collected by a flat two-dimensional detector (CCD camera), while the fluorescence data were collected by an energy dispersive Ge (Li) detector with an energy resolution of 200 eV.

The positions of the oxide-metal and oxide-water interfaces were determined by monitoring Zr L line fluorescence counts as the sample was translated across the beam. The lower density of zirconium atoms in the oxide than in the metal results in a slight reduction in Zr L intensity as

the micro-beam is moved from the metal to the oxide. This allowed the determination of the oxide location. The distance between the oxide-metal interface and the oxide-water interface measured by this method was in good agreement, to within 0.5 μm , with optical determination of the oxide thickness. Figure 4.11 shows two of these fluorescence plots across the oxide layer.

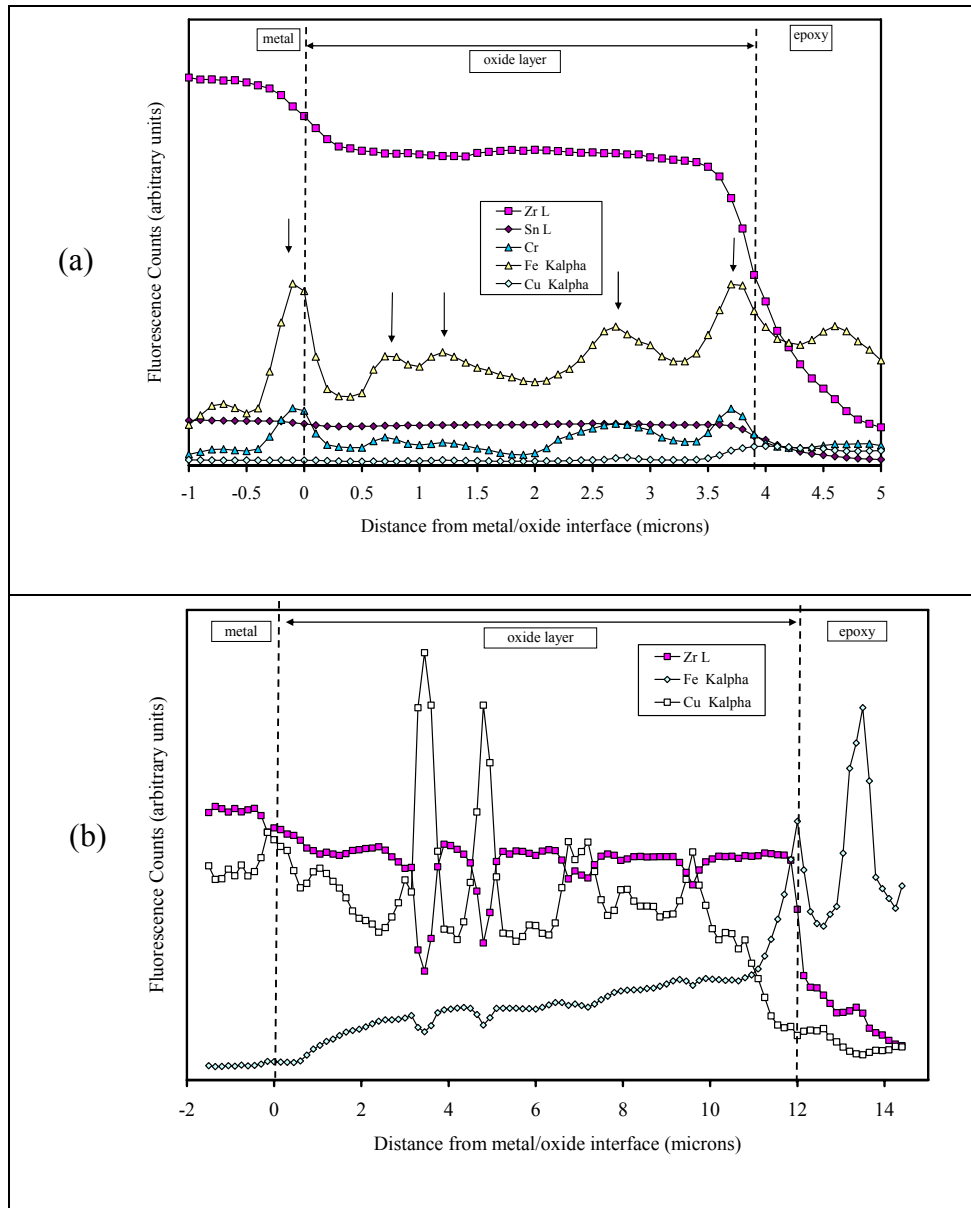


Figure 4.11: X-ray fluorescence plots obtained as a function of distance from the oxide metal interface for oxides formed on (a) Zircaloy-4 and (b) Zr1.0Cu0.5Mo in 360°C water.

Both plots show the concentrations of the alloying elements of interest (Zr, Fe, Cu and Sn). In each case the pink squares represent the concentrations of Zr. The oxide layer is noticeable because the Zr counts diminish to a lower plateau at the place marked oxide-metal interface and to zero at the oxide-water interface. The first plot, for Zircaloy-4, shows a protective oxide, with an even Zr plateau decreasing at the water interface. The thickness measured (about 4 microns) corresponds well to the weight gain measured. It is noticeable also that the Sn profile is constant

both in the oxide and in the metal, so there is no segregation of Sn to either interface. For Fe, in Zircaloy-4 there are $Zr(Cr,Fe)_2$ intermetallic precipitates which can be seen in the profile (places where both Fe and Cr increase). In contrast the oxide shown in (b) is from a non-protective oxide and it shows diminution in Zr counts related to the presence of cracks. It should be noted that the epoxy used contains Cu, which shows very prominently in the plots, since the energy is just above the Cu edge. Because the epoxy gets into the cracks, high Cu counts are seen there. Further, although the alloy contains no Fe it shows an iron concentration from the autoclave. The Fe profile is augmented all through the oxide layer, indicating that it is porous and non-protective.

The close match between the fluorescence plots and the thickness of the oxide layers measured by microscopy gives confidence that the oxide locations examined in microbeam synchrotron radiation correspond to the actual values.

Processing and Integration of Diffraction Data

Diffraction patterns are acquired at each position as the beam is scanned across the oxide cross section. A typical diffraction pattern from powder zirconia is shown in Figure 4.12. The standards were used to align the beam and make a one-to-one correspondence between location in CCD and two-theta angle.

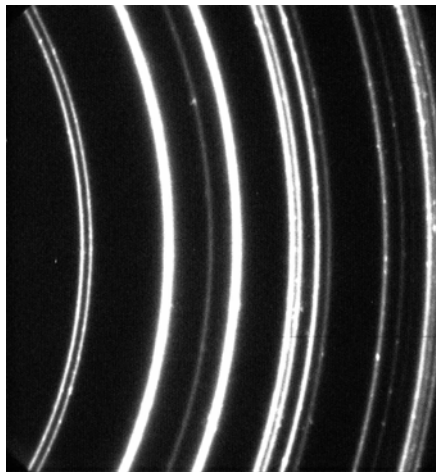


Figure 4.12: Diffraction pattern obtained from powder monoclinic ZrO_2 standard.

To obtain quantitative diffraction data, the digital data obtained from the two-dimensional detector were integrated over the elliptical sections for a fixed azimuthal angle, and the appropriate Lorentz and polarization correction factors were applied [6]. Following the integration and above corrections, a plot of diffracted intensity versus two-theta angle was obtained at each location analyzed. Figure 4.13 shows a plot of diffracted intensity versus two-theta angle for the monoclinic ZrO_2 standard shown in Figure 4.12. As shown in Table 4.1, the calculated peak positions for the monoclinic planes agree quite well with the literature values (within a few hundredths of degree).

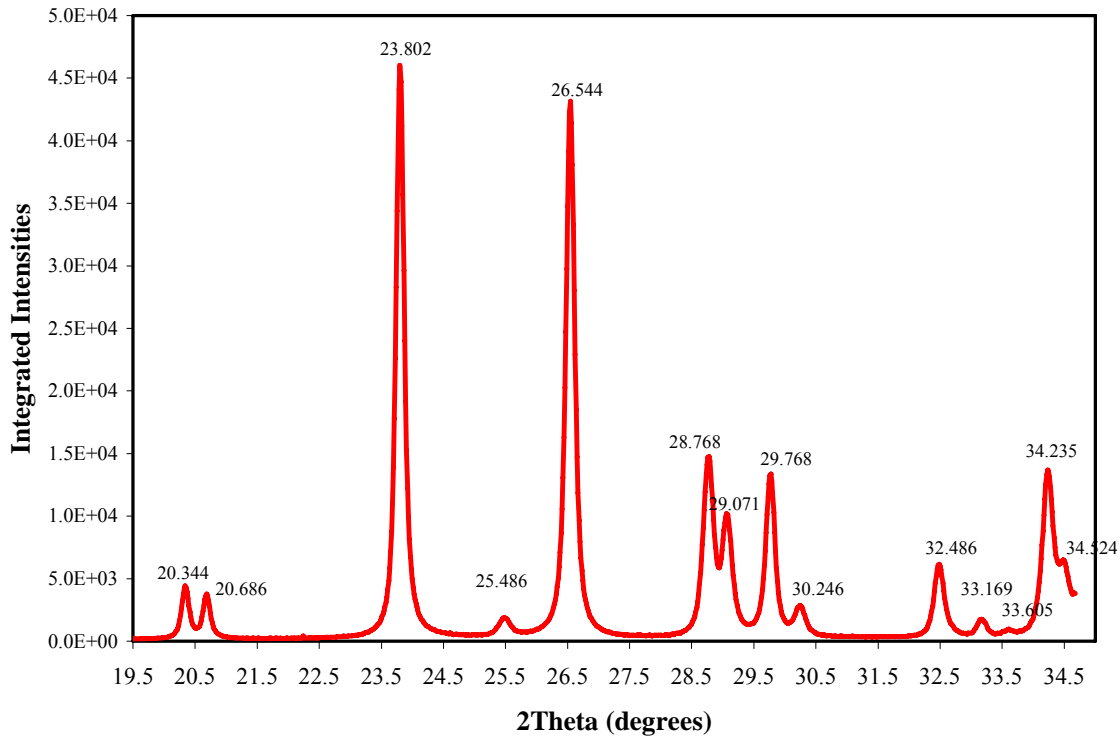


Figure 4.13: Plot of intensity versus two theta angle corresponding to the integration of the diffraction pattern shown in Figure 4.12.

Table 4.1: Comparison of observed peak positions with literature values for powder monoclinic ZrO_2 .

<i>peaks</i>	<i>Observed (degrees 2-theta)</i>	<i>PDF 37-1484 (2-theta degrees)</i>	<i>Difference (2-theta degrees)</i>
m(110)	20.344	20.327	0.017
m(011)	20.686	20.660	0.026
m(-111)	23.802	23.797	0.005
m(111)	26.544	26.558	-0.014
m(200)	28.768	28.811	-0.043
m(020)	29.071	29.003	0.068
m(002)	29.768	29.773	-0.005
m(-201)	30.246	30.276	0.030
m(102)	32.486	32.471	0.015

It is possible then to scan the beam across the oxide layer, and by stacking the plots such as shown in Figure 4.13, to generate intensity versus two theta angle plots as a function of distance for the oxide layers generated in this study. The peaks were indexed and used to identify the various different phases present in the oxide, as discussed below. Figure 4.14 shows an example of such a plot, generated for an oxide formed on $Zr_{1.5}Nb$ in pure water.

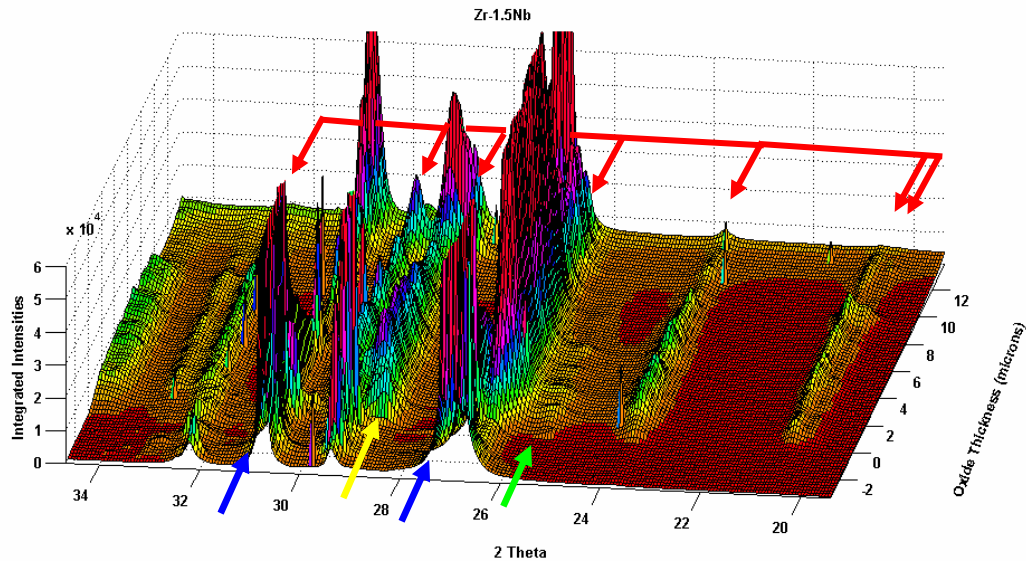


Figure 4.14: Diffraction intensity versus two theta diffraction angle versus position in the oxide layer for an oxide formed on Zr1.5Nb, in 360°C water. The monoclinic ZrO_2 peaks are in red, the bulk ZrO_2 tetragonal 101 peak is in green, the suboxide peaks in blue and the interfacial $[002]_T$ peak in yellow.

The plot shows three distinct regions: the metal, the oxide-metal interface and the oxide. Peaks characteristic of hcp Zr are visible in the metal with very high intensities, while in the oxide peaks associated with monoclinic ZrO_2 and one peak of tetragonal ZrO_2 are observed. In the interface region, additional peaks are seen that are associated with the interfacial tetragonal phase discussed below and suboxide peaks.

In this way the diffraction and fluorescence information that can be obtained from these plots can be compared from (i) alloy to alloy, (ii) within the same alloy at different stages of the corrosion process and (iii) at 360 C and 500 C. These features are discussed in the next few sections, and in context of previous observations performed on commercial Zr alloys. The information obtained is described in the following.

4.3.1. Phases present in the bulk of the oxides and overall orientation

As also seen in the frontal diffraction texture studies, the structures of oxides were quite similar, from alloy to alloy and at the two test temperatures. However, there were some important differences that distinguish protective and non-protective oxide layers, especially at the oxide-metal interface.

For all the oxides studied, the dominant oxide phase in the bulk of the oxide (away from the oxide-metal interfaces) was monoclinic ZrO_2 , with small amounts of tetragonal phase. As seen in section 4.2, the oxide layers were heavily textured. The monoclinic oxide peak intensities were far from the random powder texture. In particular the $[200]_M$ peak intensity was almost invariably low, which is consistent with the previously determined oxide growth orientation near the $\bar{3}01_M$ direction.

The differences in oxide structure for protective and on-protective oxides were notable and consistent, especially at the oxide-metal interface. These differences will be described in the following sections. The differences in oxide structure between oxides formed at 360°C and at 500°C were mostly of degree, that is, the structures of protective oxides formed at low and high temperature were similar.

Structure of the oxide-metal interface

The oxide-metal interface is of great interest to understanding the corrosion process since this is where new oxide gets formed, and where the barrier or dense layer of the oxide is located, which controls the corrosion rate. Changes to the microstructure of the oxide-metal interface will affect the overall corrosion process.

As seen previously, the oxide-metal interface is different from the bulk of the oxide and from the metal, in various respects, especially on the protective oxides. On the metal side, a sub-oxide region is detected that extends to variable extents into the metal. This sub-oxide layer is detected by metallographic examination, especially for oxides formed at high temperature and by energy dispersive x-ray spectroscopy in the SEM. It is also detected by characteristic sub-oxide diffraction peaks observed as shoulders on the metal peaks, and which are only present in the region in the metal next to the oxide-metal interface.

In addition, the overall percentage of the tetragonal ZrO₂ phase in the oxide is higher at the oxide metal interface than in the bulk of the oxide. Other researchers have indicated that in the first stages of oxidation the first oxide observed is the tetragonal oxide later transforming to monoclinic [13], and in previous research papers we have indicated that during the advancement of the oxide in the protective regime, the new oxide is formed first as tetragonal grains which later transform to monoclinic when their size reaches 20-30 nm [1].

These observations were confirmed in the present study. Figure 4.15 shows the tetragonal fraction for various model alloys in this study, calculated according to the Garvie Nicholson formula [14, 15]:

$$f_T = \frac{I_{101_r}}{I_{111_M} + I_{101_r} + I_{\bar{1}\bar{1}\bar{1}_M}} \quad (4.1)$$

where the I_{hkl} are the measured intensities of the corresponding tetragonal and monoclinic peaks. The calculation takes into account the oxide texture as described in [1].

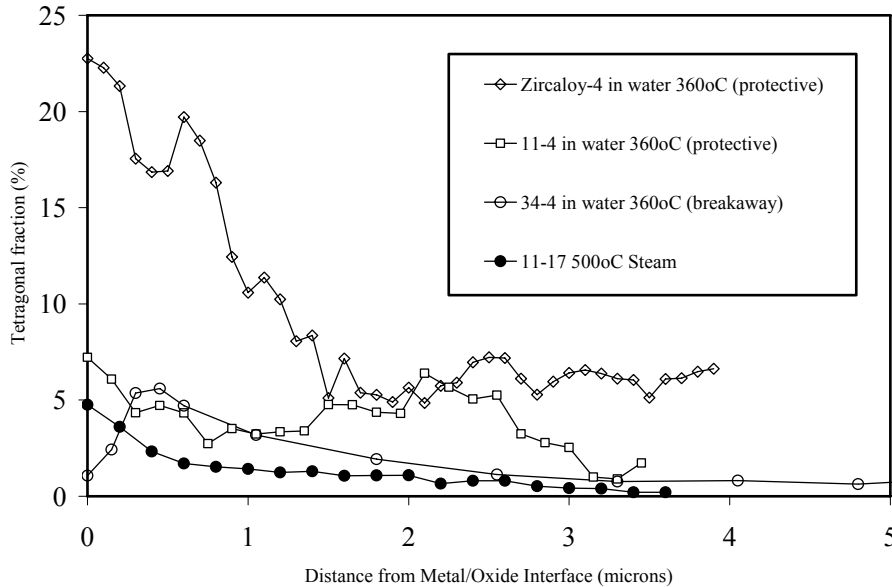


Figure 4.15: Tetragonal Fraction for oxide layers formed on various model alloys as a function of distance from the oxide metal interface.

Another remarkable observation is that some of the tetragonal phase formed at the interface (as distinct from the tetragonal phase that forms in the bulk) has a strong orientation relationship both with the metal and with the subsequent monoclinic oxide that forms away from the oxide metal interface. This has been previously observed and dubbed a highly oriented tetragonal phase, and it has been suggested that it is a precursor phase to the monoclinic phase that forms subsequently in the oxide [6, 7, 16]. The presence of this phase correlates almost one to one with a protective character in the oxide, that is, the highly oriented tetragonal phase is present when the oxide is protective and it is not present when the oxide is non protective. The diffraction patterns from the interface of protective oxides exhibit diffraction intensity corresponding to this phase, as shown by arrows in Figure 4.16.

Another observation is that the $[002]_T$ peak intensities often appears with mottled contrast, indicating the presence of strain at the interface.

Away from the oxide-metal interface the orientation of the $[020]_M$ peak is more random than at the oxide metal interface, indicating that the columns lose a little of the alignment that they have in the newly formed oxide. This is shown in Figure 4.16 which shows the diffraction patterns from various oxides, taken a few microns away from the oxide-metal interface.

The diffraction patterns taken at regular intervals starting at the metal, across the oxide-metal interface until the oxide-water interface can be stacked up and plotted together as done in Fig.4.14 to show the variation of phase content and oxide orientation within the oxide layer. Figures 4.17 to 4-22 show four examples of these plots (intensity versus two theta angle versus distance to the oxide-metal interface), taken from four different oxide layers, both protective and non-protective.

	Oxide-metal interface	3 microns away
Zr _{0.5} Cr (90 days in 360°C water, weight gain 955.9 mg/dm ²)		
Zr _{1.5} Nb		
Zr _{0.2} Fe _{0.1} Cr (L) (415 days in 360°C water, weight gain 55.0 mg/dm ²)		
Zr _{1.0} Cr _{0.2} Fe (150 days in 500°C supercritical water, weight gain mg/dm ²)		

Figure 4.16: Diffraction patterns from the oxide-metal interface, taken in cross section in the rolling-normal plane (transverse direction perpendicular to the sample surface) for samples and exposures indicated. A yellow outline shows the intensity from the [002]_T plane of the interfacial tetragonal phase.

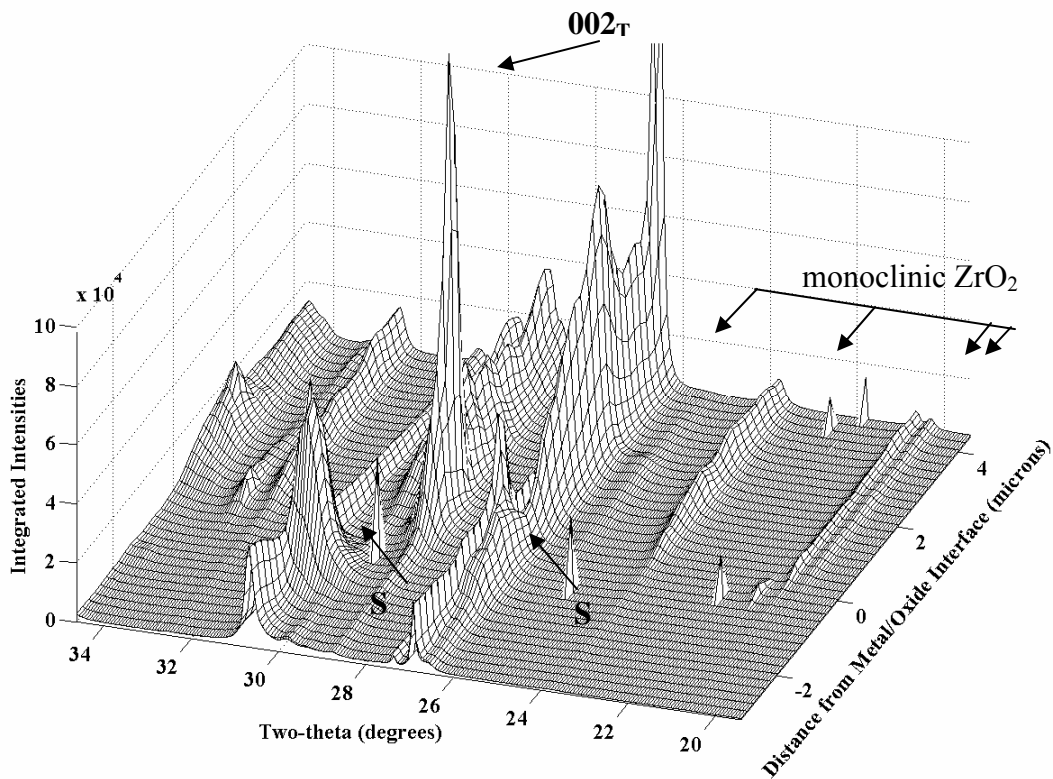


Figure 4.17: Diffraction intensity versus two theta angle versus position in the oxide for alloy 24 (Zr1.0Cr0.2Fe) corroded in 500°C supercritical water for 150 days.

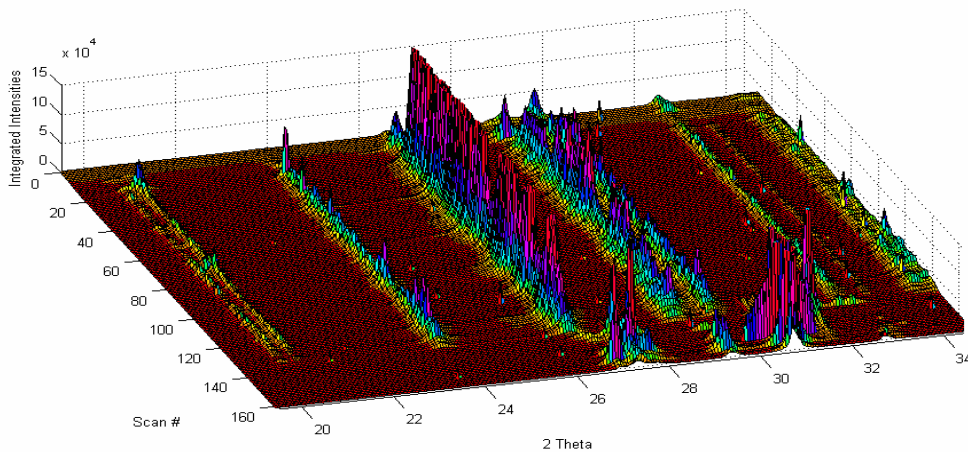


Figure 4.18: Diffraction intensity versus two theta angle versus position in the oxide for alloy Zr0.4Nb corroded in 500°C supercritical water for 300 days.

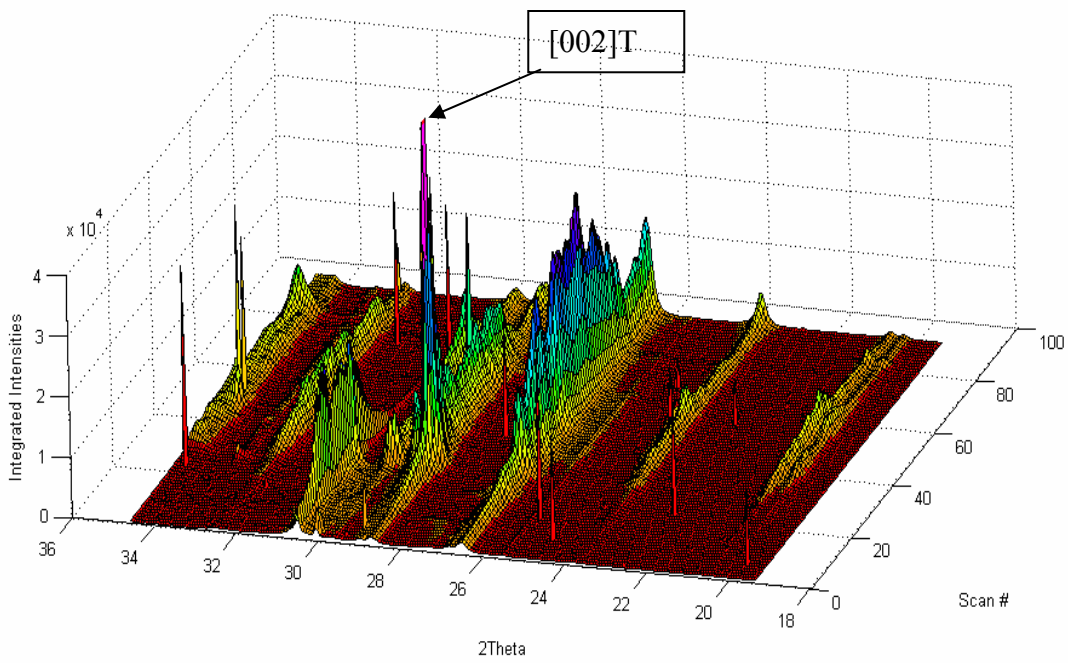


Figure 4.19: Diffraction intensity versus two theta angle versus position in the oxide for alloy 14 (Zr_{0.4}Fe_{0.2}Cr (H)) corroded in 500°C supercritical water for 150 days.

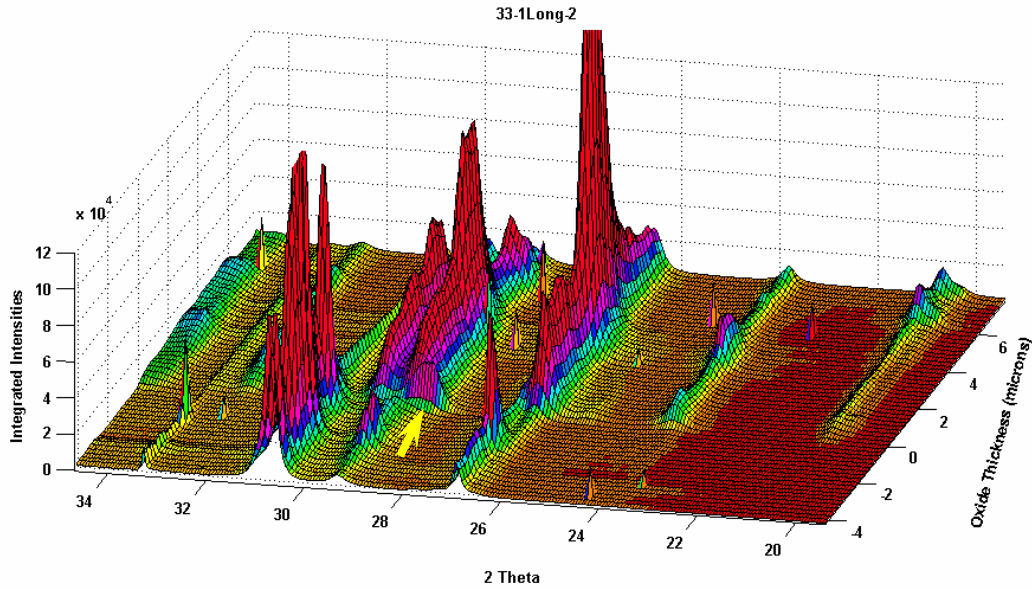


Figure 4.20: Diffraction intensity versus two theta angle versus position in the oxide for alloy 33 (Zr_{1.0}Cu) corroded in 360°C water for 409 days.

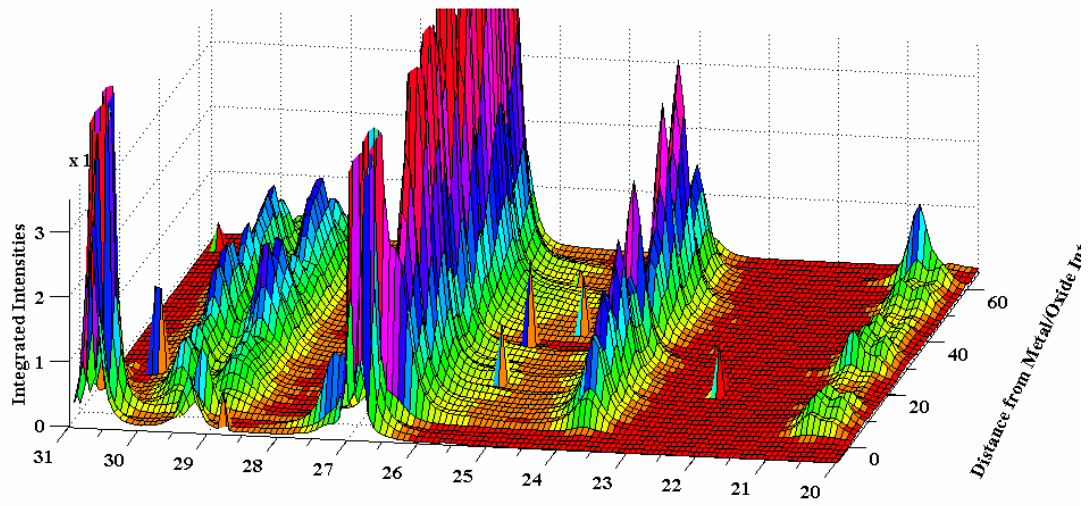


Figure 4.21: Diffraction intensity versus two theta angle versus position in the oxide for alloy 21 (Zr0.5Cr) corroded in 360°C water for 90 days.

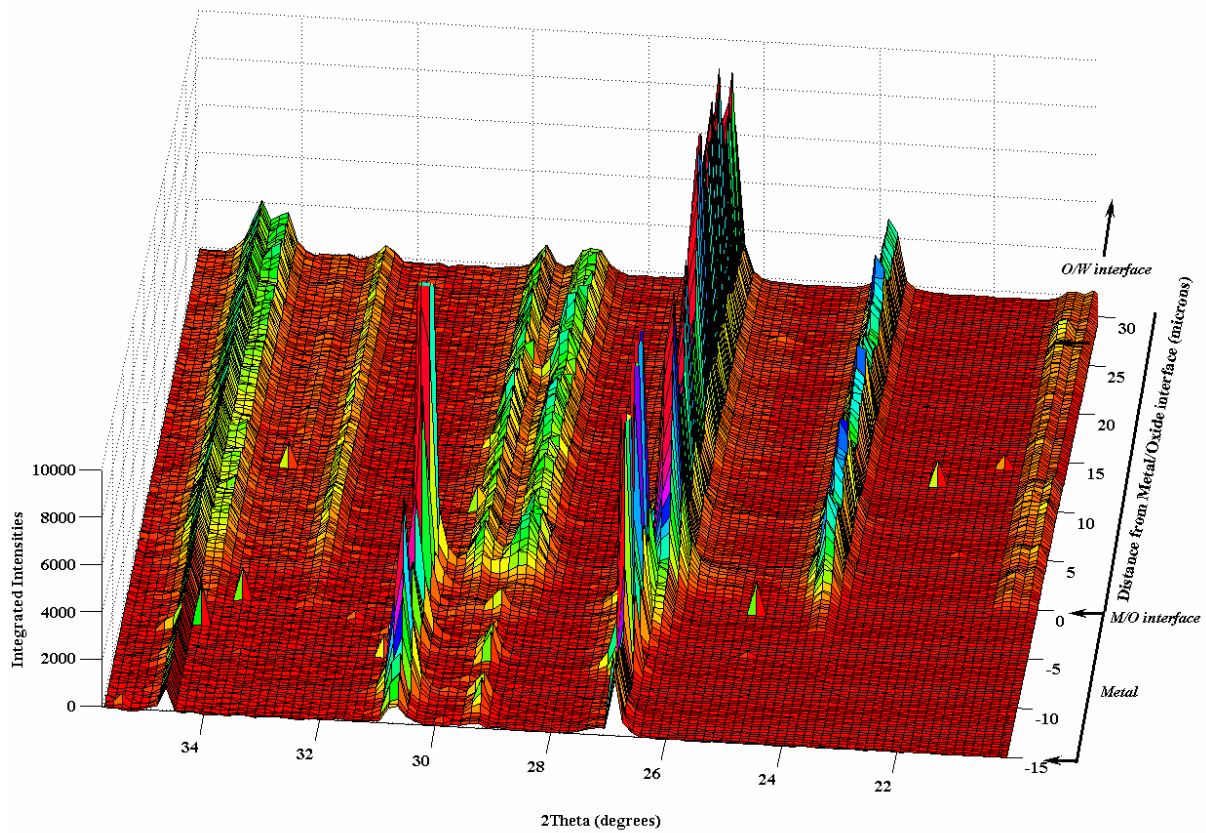


Figure 4.22: Diffraction intensity versus two theta angle versus position in the oxide for alloy 21 (Zr0.5Cr) corroded in 500°C steam.

The main differences between these series of diffraction patterns are at the oxide-metal interface. The protective oxides show the $[002]_T$ peak and the sub-oxide peaks. The $[002]_T$ peak is arrowed at the interface in the protective oxide formed on alloy Zr1.0Cu at 360 C (Figure 4.20). In the protective oxides formed at high temperature this peak is much higher as shown in Figure 4.17. The arrowed peak is very high, indicating a large volume of this phase at the interface.

Figure 4.17 shows the diffraction patterns from an oxide layer formed on alloy 24 after 150 days in supercritical water at 500°C. The oxide metal interface is at position zero, and in the negative positions, the metal peaks are indicated, with suboxide peaks indicated as “S”. In the oxide the monoclinic oxide peaks are visible. At the interface a very large peak, indicated as $[002]_T$ is shown. This peak was visible in the protective oxides seen at high temperature and absent in the oxides that were non-protective. As seen previously, the tetragonal peak is observed just ahead of the full oxide-metal interface, in the region near where the new oxide is forming. In contrast, Figure 4.18, taken from an oxide in alloy Zr0.4Nb exposed to 500°C supercritical water for 300 days shows an interface in which this peak is absent. Figure 4.19 shows an oxide layer formed on Zr0.4Fe0.2Cr (H) when exposed to 500°C supercritical water, exhibiting the a similar peak at the interface.

At lower temperature the same peak appears associated with protective oxides but is lower in intensity. Figure 4.20 shows the diffraction patterns associated with a protective oxide layer formed during exposure to 360°C water in alloy Zr1.0Cu. The peak (arrowed) is also present at the interface, but at a much lower intensity than at high temperature. Figures 4.21 and 4.22 shows two non-protective oxides generated by exposure to 360°C and 500°C respectively, in which the interfacial tetragonal phase is not present.

One possible conclusion from these observations is that the tetragonal phase formed at the interface may help align the oxide in a manner that helps minimize stresses during its growth. As such, this tetragonal phase detected at the interface would be highly aligned and may serve as a precursor phase that helps the oxide form in a more aligned fashion. It is given that to minimize stresses the oxide growth direction is near $(-301)_M$, which means that the $[020]_M$ and $[002]_M$ planes are aligned with their poles nearly normal to the oxide growth direction. It appears that a close alignment of the $[020]_M$ plane with the $10\bar{1}0_{hcp}$ plane is more favorable for stable oxide growth than a random in plane-texture of these planes, evenly distributed between the rolling and transverse directions. Because the $[002]_T$ plane is parallel to the $10\bar{1}0_{hcp}$ peak and the $[020]_M$ plane of the monoclinic phase forms parallel to the $[002]_T$ plane of the tetragonal phase, the alignment is achieved when the highly oriented tetragonal phase is present. This can also be verified in Figure 4.16 which shows that there is close alignment of the $[002]_T$ planes and the $[020]_M$ intensities along the diffraction arcs in the diffraction patterns taken close to the oxide-metal interface. This is expressed as:

$$[10\bar{1}0]_{hcp} // [002]_T // [020]_M$$

This orientation is shown schematically in Figure 4.23.

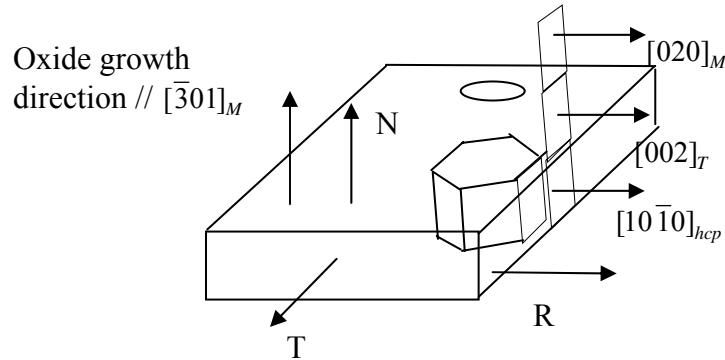


Figure 4.23: Orientation relationship of the hcp Zr metal planes and the tetragonal and monoclinic oxide planes near the oxide-metal interface in the protective oxides. R is rolling direction of the metal sheet, N is the normal direction (parallel to the oxide growth direction) and T is the transverse direction.

The interfacial tetragonal phase in the protective oxides is thus thought to induce a favorable in plane texture in which the $[020]_M$ direction of the oxide is preferentially aligned with the $10\bar{1}0_{hcp}$ planes in the metal. This alignment resulting from the interfacial tetragonal phase results in a higher ratio

$$\gamma = \frac{I_{020_M}}{I_{002_M}} \quad (4.2)$$

of diffracted intensities of the $[020]_M$ peak and the $[002]_M$ peak. This ratio was calculated for various oxides of interest and is plotted in Figure 4.24. It is clear that the ratio is higher in the protective oxides than in the non-protective oxides.

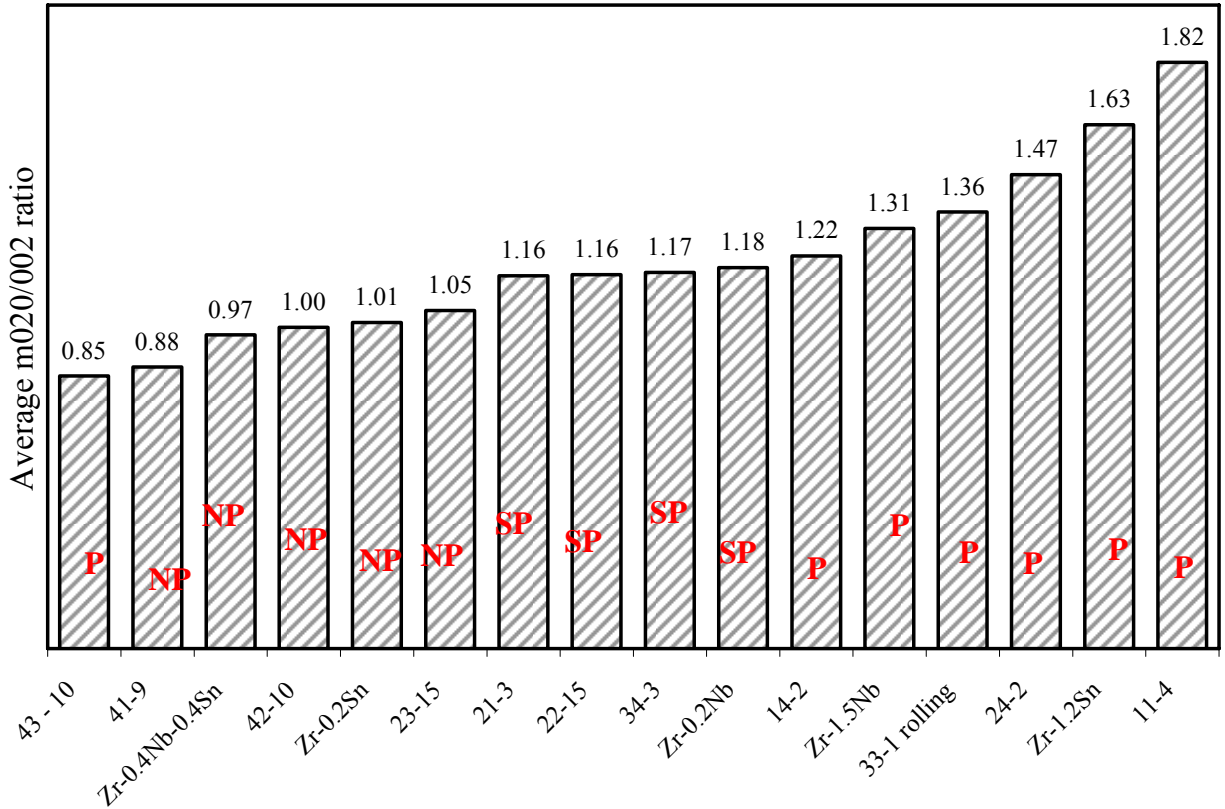


Figure 4.24: Ratio of intensities of the $[020]_M$ and $[002]_M$ oxide planes when examined in the rolling –normal sample plane (transverse direction perpendicular to surface). P indicates a protective oxide, SP semi-protective and NP non-protective.

Overall Tetragonal phase fraction level

The tetragonal phase fraction has been previously linked to corrosion behavior in Zr alloys [17, 18]. It is difficult however to separate cause and effect in this case. In previous research, we have shown that an increased tetragonal fraction did not correlate necessarily with best corrosion behavior [6]. Protective oxides of the same alloy will have higher tetragonal fraction before breakaway than after breakaway, however from alloy to alloy higher tetragonal fraction does not increase protectiveness. This trend was confirmed here. The maximum tetragonal phase fraction calculated using Equation 4.1 and corrected for texture as in [6].

The tetragonal phase fraction varied from 2% to 15-20%, and for most oxide layers, it fell between 4-8%, as seen in figure 4.25. No clear correlation was seen between protectiveness of the oxide and the overall level of tetragonal phase in the oxide.

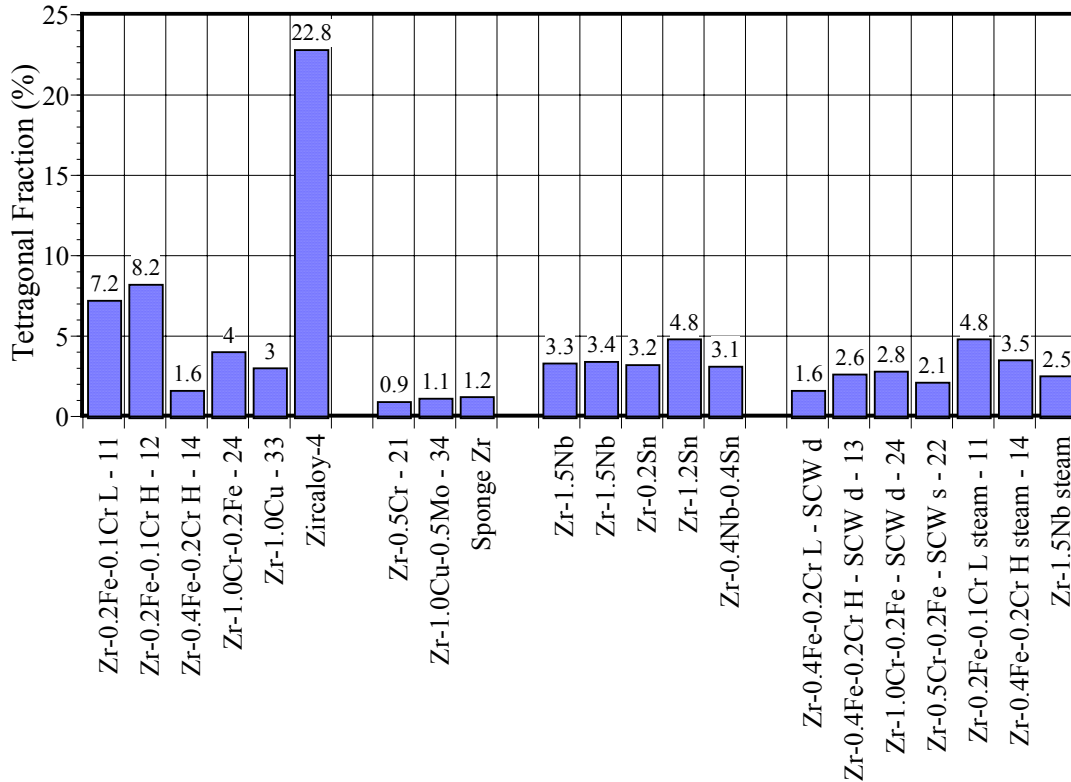


Figure 4.24: Average tetragonal fraction for various oxides formed during low and high temperature corrosion testing.

Monoclinic Grain sizes in oxides

For a given testing temperature the grain sizes calculated from the Scherer equation are similar for the oxides studied.

For oxides formed at 360°C, the tetragonal grain sizes (calculated from the broadening of the $[101]_T$ peak) are 7-10 nm and the monoclinic grains calculated either from the broadening of either the $[-111]_M$ or $[-111]_M$ peak are about 20-25 nm, as shown in Fig.4.26. The bulk of the oxide shows a more or less even grain size whereas the only variations are near the oxide-metal interfaces the calculations have greater associated uncertainties (smaller peaks, confounding metal peaks, etc.). The monoclinic grains in the alloys that contain Sn and Nb in solid solution (Zircaloy, ZrSn, ZrNb) are possibly a little smaller (17-20 nm).

Occasionally there are variations in the grain size from point to point and these are normally associated with large single grains that show up on the diffraction pattern as bright spots. It is possible that these spots are artifacts coming from previously undetected impurity phases on the surface oxide sample, or that occasionally there are large grains in the oxide amidst the smaller ones. Regardless, the overall size of the oxide grain population is close to what is shown above. For oxides formed at 500°C the monoclinic grain sizes appear to be a little bigger (about 30-35 nm from the broadening of the $[-111]_M$ peak) and about the same size for the tetragonal as the lower temperature (10-12 nm), as shown in Fig.4.27. This is consistent with the tetragonal grains transforming to monoclinic after a certain size and not growing within the oxide.

These grain sizes are in general agreement with previous determinations of grain size in oxides in commercial alloys using the synchrotron radiation.

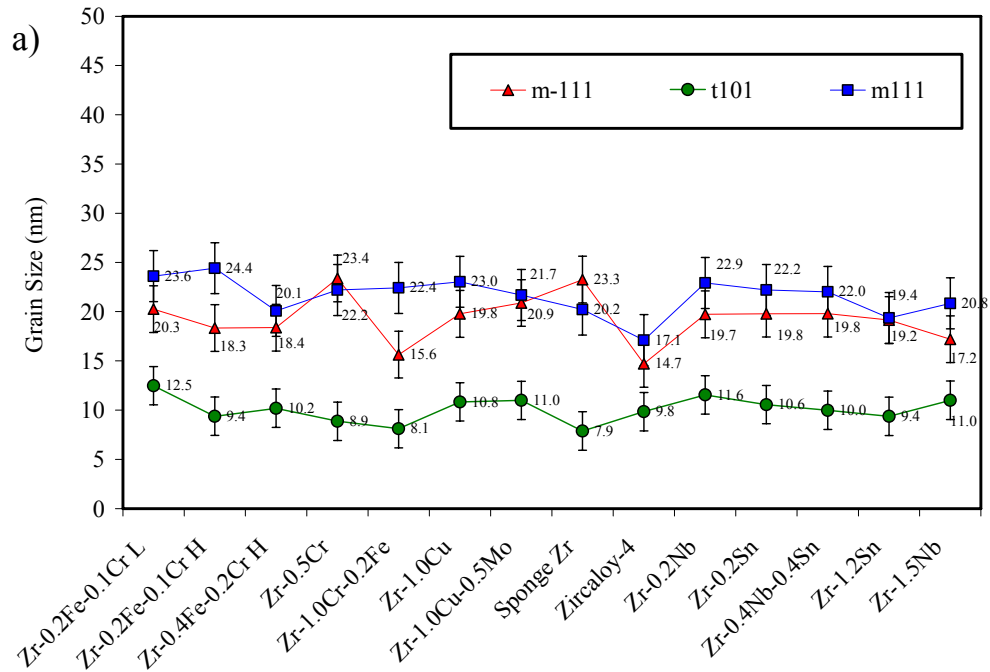


Figure 4.26: Average grain sizes calculated according to the Debye Scherrer formula for in various oxide layers formed during 360°C corrosion testing.

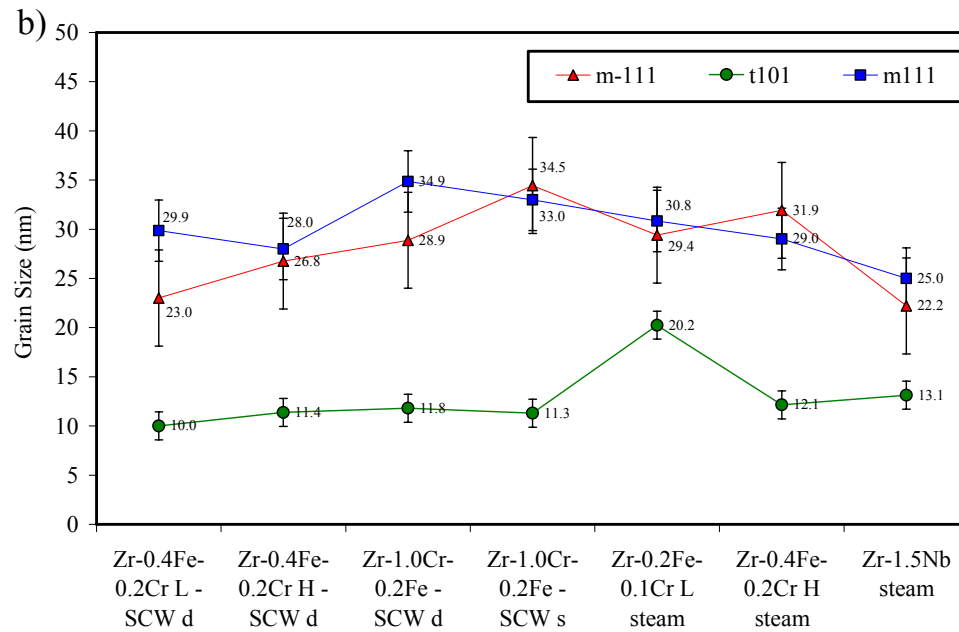


Figure 4.26: Average grain sizes calculated according to the Debye Scherrer formula for in various oxide layers formed during 500°C corrosion testing.

Microstructure characterization of the oxide by TEM

The oxide growth mechanism on Zr alloys is affected by the various factors such as microstructure, crystallographic structure, oxide texture and second phase particles embedded in oxide. TEM has been considered to be a proper technique to obtain the oxide grain size and shape, crystal structure of the grains, and the characteristics of the second phase particles. The objective of TEM observation for the oxide is to assist in the interpretation of the oxide growth mechanism of the model alloys with different alloying element in different corrosion environments.

The sample preparation of the cross-sectional oxide sample was carried out according to the following procedure. (1) Two segments with about 3 mm width were cut from the corroded samples and then glued together on the corroded surfaces. (2) This piece was inserted into a stainless steel tube with 4mm inner diameter using the G1 epoxy-type glue and then cured at 100C for 60 minutes. (3) The cured tube was sliced into the 0.3 mm thick disk by a low speed cutter. (4) The disk samples were ground from 1200 grit abrasive paper to 0.5 μm diamond cloth on both sides until the thickness was thinned to approximately $10\pm 2 \mu\text{m}$. (5) The polished samples were glued on to the Cu grid and then finally thinned by ion milling. The prepared samples were observed using the 200 keV TEM (JEOL FX 2) in KAERI.

Figure 4.28 shows the general morphology of the two oxides on Zr-0.4Nb corroded to 90 and 300 days in 360C water, respectively. The columnar oxide grains grow in the perpendicular direction to the oxide/metal interface in the thin as well as thick oxides. Several lateral cracks were observed in the thick oxide layer, and the equiaxed grains were largely formed on the area of outer water/oxide and near the lateral cracks in the thick oxide as shown in Fig. 28 (b). It was suggested that the lateral cracks and the equiaxed grains were easily formed with increasing the oxide thickness.

Figure 4.29 shows TEM microstructures of the oxides on Zr-0.4Nb, Zr-1.5Nb and Zr-1.0Cr-0.2Fe alloys corroded to 60 days in 500C supercritical water. Since the corrosion rate in the supercritical water is much higher than that 360C water, the oxide thickness of two Nb-containing Zr alloys was thicker than 30 μm just after 60 days. At the equal corrosion time, the oxide thickness of Zr-1.5Nb alloy was thinner than that of Zr-0.4Nb alloy. Both columnar and equiaxed oxide grains were observed in the two Nb-containing Zr alloys formed. The overall oxide morphology characteristics were shown to be similar both in 360C water and 500C supercritical water. The area of columnar oxide grains of Zr-1.5Nb alloy was higher than that of Zr-0.4Nb alloy at the same corrosion time of 60 days. In both alloys, the lateral cracks in the oxides were randomly distributed in the oxide layer and the equiaxed grains were observed more frequently near the cracks. On the other hand, the oxide thickness of Zr-1.0Cr-0.2Fe alloy was very thinner than those of Nb-containing alloy at the equal exposure time. The area of columnar oxide grains of Zr-1.0Cr-0.2Fe alloy was higher than that of columnar oxide grains of Zr-1.5Nb alloy and the lateral cracks were not observed in the oxide formed on Zr-1.0Cr-0.2Fe alloy.

Figure 4.30 shows the characteristics of the oxide on Zr-1.5Nb alloy corroded in 500C supercritical water more precisely. The columnar structure grains were well developed in the inner area of the oxide and the columnar and small equiaxed grains were mixed in the outer area of the oxide. From the selected area diffraction pattern analysis, it was found that the (200) or (020) monoclinic ZrO_2 reflections were matched with the some columnar oxide grains in the oxide. In the diffraction pattern taken from inner area region of oxide, the (200) monoclinic reflections were stronger and almost well oriented. However, in the diffraction pattern taken from the middle area in oxide, the (200) monoclinic reflections are weaker and the angle between (200) and (020) monoclinic ZrO_2 are larger than in case of the inner area region. In this case, the columnar grains were transformed to the small equiaxed grains. It was assumed that columnar structure was stabilized by the well aligned oxide orientation of (200) and (020) monoclinic ZrO_2 phase.

The characteristics of the second phase particle incorporated into the oxide of Zr-1.5Nb alloy corroded for 60 days in supercritical water was shown in Figure 4.31. At the low magnification image shown in Figure 4.31 (a), lateral cracks were randomly distributed in the oxide. From the results of EDS and SAD patterns of the incorporated second phase particles in the oxide, the incorporated second phase particles in the oxide were revealed as the amorphous structure type even at the position more than 28 μm away from the metal/oxide interface. This type of incorporated second phase particles was thought to be resulted from the beta-Nb contained in Zr-1.5Nb alloy before corrosion test. Since the lateral cracks were not observed near the oxidized second phase particles, it was thought that the crack formation was not affected by the late oxidation of the incorporated beta-Nb.

From the TEM observation on the various oxides formed on model alloys, the corrosion resistance of the model alloys was closely related to the oxide morphology. The fraction of columnar grains in oxides was increased in the model alloys showing the higher corrosion resistance both in 360C water and in 500C supercritical water. The stability of the columnar grain was closely related to the texture of the oxide: The strong orientation of monoclinic (200) and (020) was well matched with the columnar grains. The role of second phase particles during the corrosion was not clear because the correlation was not obtained between the incorporated second phase particles and the oxide morphology characteristics such as lateral cracks and columnar grains.

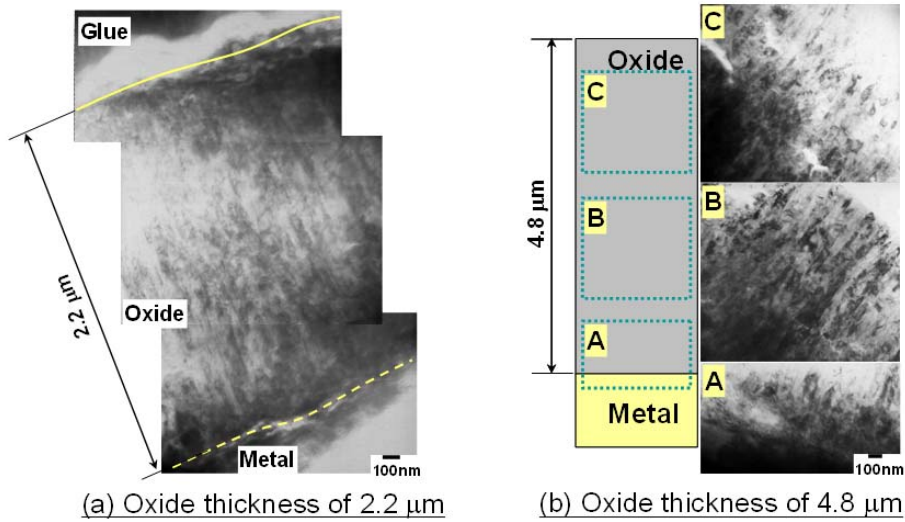


Figure 4.28: TEM microstructures of the oxides on Zr-0.4Nb corroded up to oxide thickness of (a) 2.2 mm and (b) 4.8 mm in 360C water.

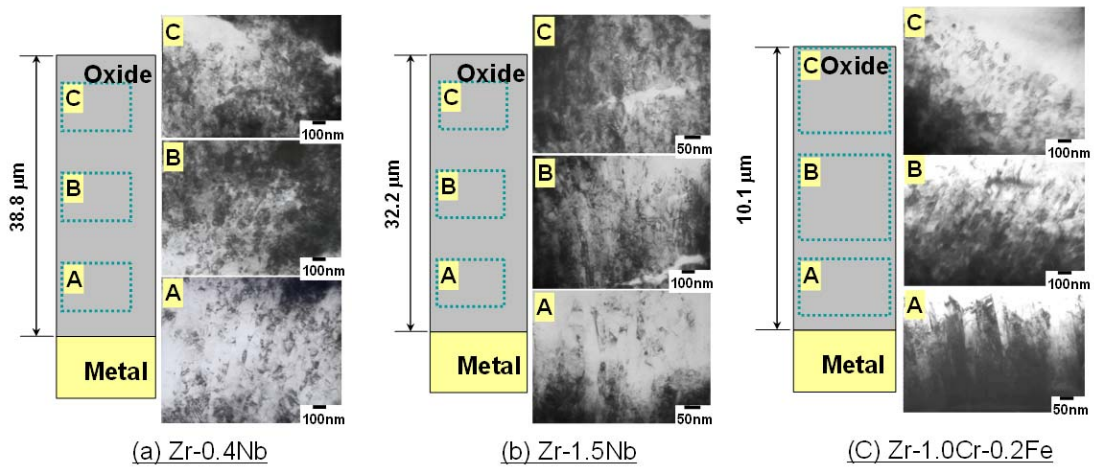


Figure 4.29: TEM microstructures of the oxides on (a) Zr-0.4Nb, (b) Zr-1.5Nb and (c) Zr-1.0Cr-0.2Fe corroded up to 60 days in 500C supercritical water.

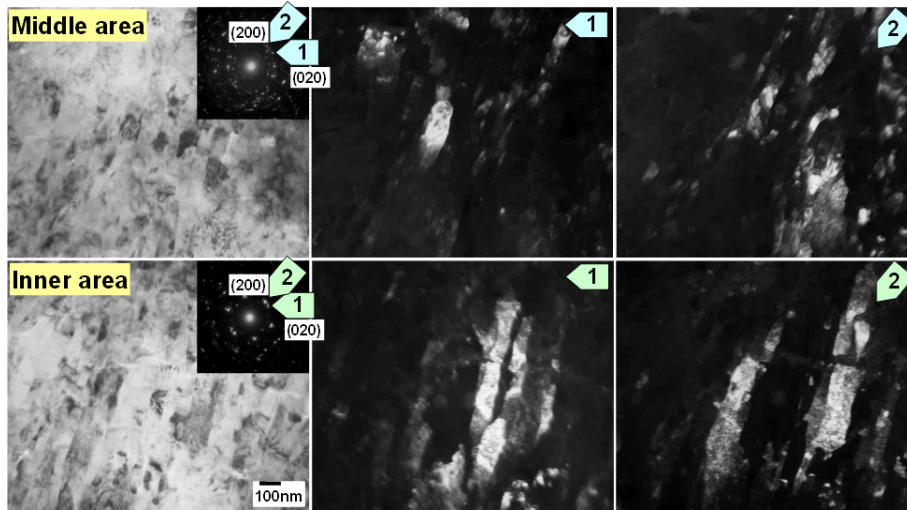
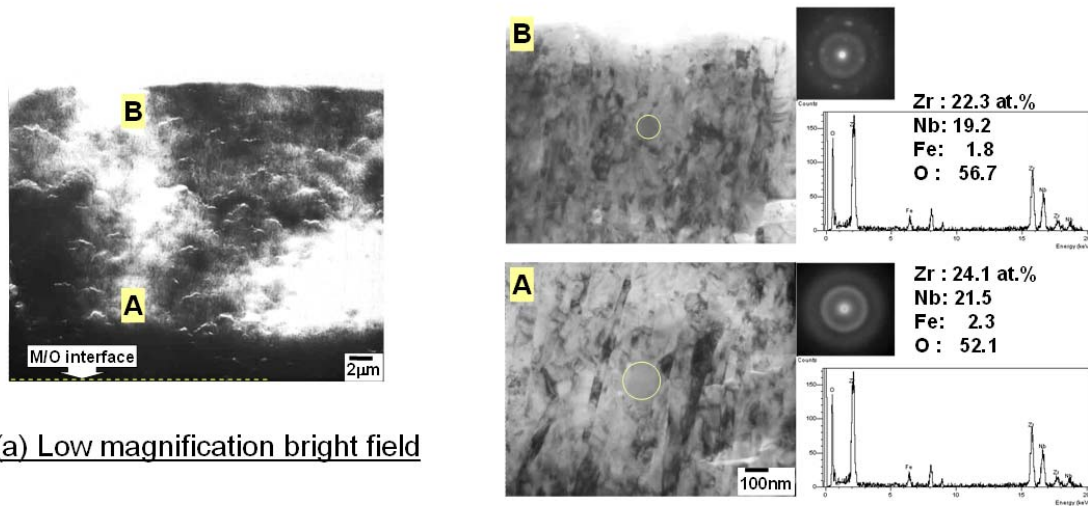


Figure: 4.30: Oxide characteristics of Zr-1.5Nb corroded in 500C supercritical water.



(a) Low magnification bright field

(b) Precipitate in oxide

Figure 4.31: The characteristics of the second phase particle incorporated into the oxide of Zr-1.5Nb alloy corroded for 60 days in supercritical water.

Nano-indentation on the oxide

Nano-indentation test on the oxide was conducted to investigate the mechanical properties of the oxide in the model alloys more quantitatively. The objective of the nano-indentation test was to obtain the oxide property such as the nano-hardness, the elastic modulus along the oxide thickness and evaluate the oxide stability in terms of the mechanical properties of the oxide.

The model alloys tested was Zr-0.4Nb, Zr-1.5Nb, Zr-1.0Cr, and Zr-1.0Cr-0.2Fe corroded in 360C water and in 500C supercritical water. The specimens after autoclave testing were sectioned by the low speed cutter, mounted perpendicular to the sectioned plane, and ground with up to 4000 grit abrasive paper. In order to minimize scratches caused by the spalled oxide during grinding, the specimens were ground in parallel direction with oxide/metal interface to reduce the scratches on the oxide by the oxide debris. After grinding, the specimens were finally polished by 0.05 μ m alumina cloth to reduce the surface roughness prior to the nano-indentation. Nano-indentation test was performed at the MTS nano-indentor XP model which has a displacement resolution of 0.01 nm, a maximum indentation depth of 500 μ m, and a maximum load limit of 500 mN. Berkovich-type indenter was used in this study. The specimen was indented then unloaded to obtain load-displacement curve. 20 points per specimen was indented along the inclined direction to the oxide/metal interface with an interval of 50 μ m. The oxide modulus and the nano-hardness were measured at each point by the load-displacement curve. As the oxide thickness of the model alloy after corrosion was too thin to measure exact value at each local point, nano-hardness and oxide modulus averaged at each local point were used in this study, except for the specimen exposed at the supercritical water in which oxide was thick enough to obtain local values.

Figure 4.32 shows the effect of Nb contents on the average nano-hardness property and the weight gain in 360C water. Weight gain increased as the exposure time elapsed. On the other hand, little effect of Nb addition appeared in case of 360C water corrosion. The effect of both the alloying element and the water chemistry on the oxide stability of Zr-Cr-Fe alloy is shown in Figure 4.33. Significant increase of the oxide hardness was observed when 0.2 wt% of Fe is added. Corrosion notably decreased from 277 mg/dm² in Zr-1.0Cr to 62 mg/dm² in Zr-1.0Cr-0.2Fe alloy after 390 days corrosion in 360C water. This indicates that oxide stability was greatly increased even by small amount of Fe addition to result in the increase of corrosion resistance. In terms of environment effect, however, negligible change of the nano-hardness appeared regardless of the water chemistry such that the weight gain increased at the supercritical water compared to the 360C water environment.

The local nano-hardness profile across the oxide thickness was obtained for the thick oxide on both Zr-0.4Nb and Zr-1.5Nb corroded in supercritical water as shown in Figure 4.34. The nano-hardness value of the metal part is approximately in 3 GPa. On the other hand, oxide nano-hardness value was in the range of 8 to 14 GPa. Nano-hardness changed so abrupt that one can easily find the interface between the oxide and the metal. Although some points showed anomalous value at which the tip of the indenter is assumed to be trapped by a circumferential or lateral crack, the profiles of nano-hardness generally decreases within 10 μ m then came close to the stable value. Nanohardness value at the outer side of oxide was 8 GPa in Zr-0.4Nb alloy, whereas 11 GPa in Zr-1.5Nb alloy. Their weight gain was 582 mg/dm² in Zr-0.4Nb alloy, 483

mg/dm² in Zr-1.5Nb alloy after 60 days corrosion in supercritical water. The weight gain as well as the related oxide thickness was reduced as the Nb content increased. The slope of nano-hardness was more rapid in Zr-0.4Nb alloy than Zr-1.5Nb one. In other word, the local nano-hardness distribution across the oxide thickness was more inhomogeneous in Zr-0.4Nb than Zr-1.5Nb. Although nano-hardness value at the oxide-metal interface was similar in both alloys, the changes of nano-hardness were abrupt in Zr-0.4Nb alloys such that the nano-hardness at the outer oxide in Zr-0.4Nb was smaller than in Zr-1.5Nb alloy.

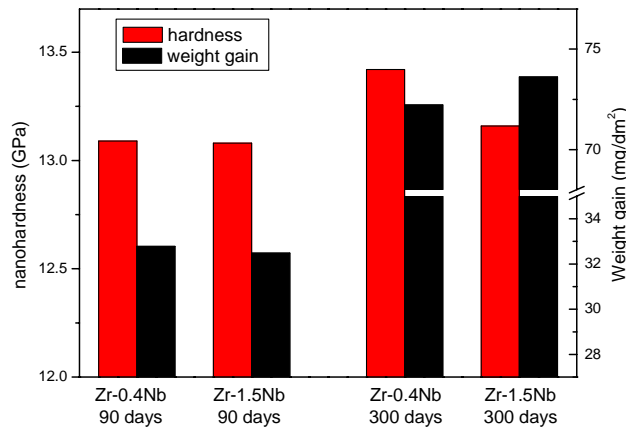


Figure 4.32: The effect of Nb content on the average nano-hardness of the oxide formed in 360C water.

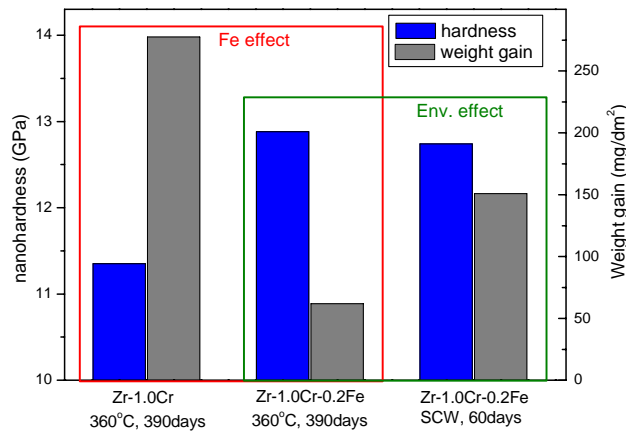


Figure 4.33: The effect of Fe addition on the average nano-hardness

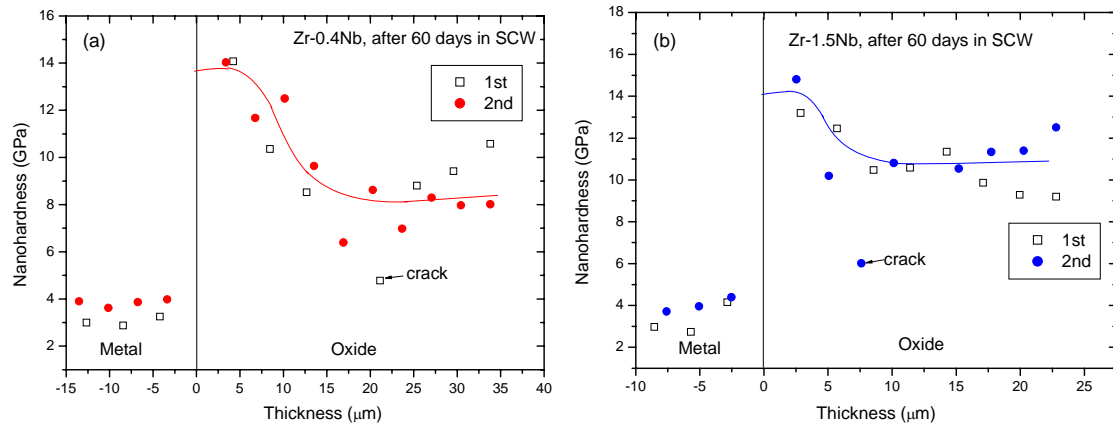


Figure 4.34: Local nano-hardness profile of the oxide on (a) Zr-0.4Nb and (b) Zr-1.5Nb corroded up to 60 days in supercritical water.

Electrochemical Impedance Spectroscopy on the oxide

In general, Zr oxide consisted of the porous non-protective outer layer and the impervious protective inner layer. The penetration of the electrolyte with oxygen ion through the open pore or crack of the oxide layer reduce the electrical resistance of the oxide layer and is one of the causes for the accelerated corrosion. Electrochemical impedance spectroscopy (EIS) is suitable method to evaluate these properties without destruction of the oxide. The oxides on the model alloys were analyzed by EIS to evaluate the oxide properties and to correlate with the corrosion properties of the alloys.

EIS measurement were carried out using an impedance spectrum analyzer (IM6, Zahner electric, Germany) which was connected to three-electrode electrochemical cell (K0235 Flat Cell, EG&G PAR). The EIS spectra were obtained at open-circuit potential (OCP) of the working electrode (Zr oxide) in 0.01 M H₂SO₄ + 0.1 M K₂SO₄ solution at 25°C. A platinum grid was used as a counter electrode and a saturated calomel electrode (SCE) connected to the cell by a salt bridge served as a referenced electrode. AC signal was scanned from 5 x 10⁶ Hz to 5 x 10⁻⁴ Hz with a amplitude of 10 mV. Before the EIS measurement, the oxide was soaked in a test solution as an electrode for 0.5, 1, 2 and 3 days. Zr-0.4Nb, Zr-1.5Nb and Zr-1.0Cr-0.2Fe alloys corroded in supercritical water were selected for EIS. The thin and thick oxide were sampled at 6 day and 60 days and tested by EIS. Figure 4.35 shows Bode plots with soaking time for the thick oxide of Zr-0.4Nb corroded up to 60 days in supercritical water. Impedance and phase angle lower than 10 Hz changed significantly with soaking time which means the electrolyte penetrated into the pores or cracks of the oxide layer. However, such a tendency was not observed in the thin oxide, which means the thin oxide has more protective nature as compared to the thick oxide.

Figure 4.36 shows Bode plots of 3 day-soaked thin and thick oxide of Zr-0.4Nb corroded in supercritical water. The oxide thickness of the thin and thick oxide calculated from the weight gain was 3.8 and 38.8 μm, respectively. EIS spectrum for the thin oxide shows higher electrical resistance (impedance) and higher phase angle at low frequency (<10 Hz) when compared to the thick oxide, which means the thin oxide has a higher protectiveness than the thick oxide. From the observation on the cross-section of the oxide, the vertical crack penetrated from the surface to about 90% thickness was found along with many small pores. The thick oxide could be interpreted as a double layer structure and its low electrical resistance would be caused by the fact that the thick outer oxide has many open pore and/or crack.

Figure 4.37 shows the EIS spectra of Zr-1.5Nb and Zr-1.0Cr-0.2Fe alloys corroded in supercritical water condition for 60 days. EIS spectra of the Zr-1.0Cr-0.2Fe alloy shows higher electrical resistance and higher phase angle at low frequency (<10 Hz) than that of Zr-1.5Nb alloy. Especially, phase angle of Zr-1.0Cr-0.2Fe alloy has about 90 in a wide range of frequency (10⁻¹<f <10⁴ Hz) which means the oxide layer has capacitive properties and high protectiveness. Table 5 summarizes the oxide thickness, electrical resistance and specific resistance. The specific resistance of the thin oxide was orders of magnitude higher than that of thick oxide. And Zr-1.0Cr-0.2Fe alloy has higher specific resistance than that of Nb-containing Zr alloys. The corrosion rate of Zr-1.0Cr-0.2Fe alloy was very lower than Nb-containing Zr alloys in supercritical water. It implies that the specific resistance of the oxide was closely related with the corrosion rate of the alloy.

Table 4.2: Oxide thickness and specific resistance of Zr alloys corroded in supercritical water

<i>Alloy</i>	<i>Corrosion time (days)</i>	<i>Oxide thickness (μm)</i>	<i>Electrical resistance (Ω)</i>	<i>Specific resistance (Ωcm)</i>
Zr-0.4Nb (thin)	6	3.8	1.50E+09	3.95E+05
Zr-0.4Nb (thick)	60	38.8	1.30E+05	3.35E+00
Zr-1.5Nb	60	32.2	2.60E+09	8.07E+04
Zr-1.0Cr-0.2Fe	60	10.1	5.90E+10	5.84E+06

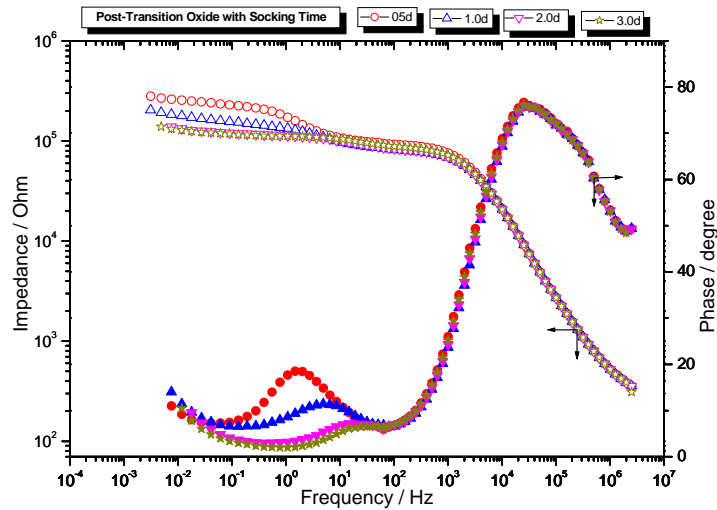
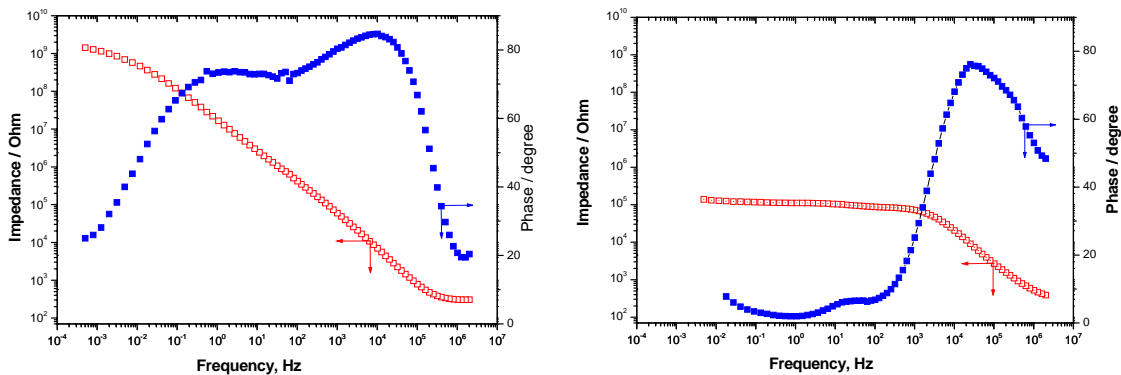


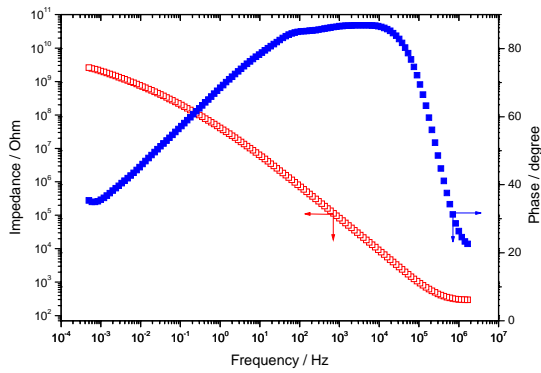
Figure 4.35: Bode plots with soaking time for the thick oxide of Zr-0.4Nb corroded up to 60 days in supercritical water.



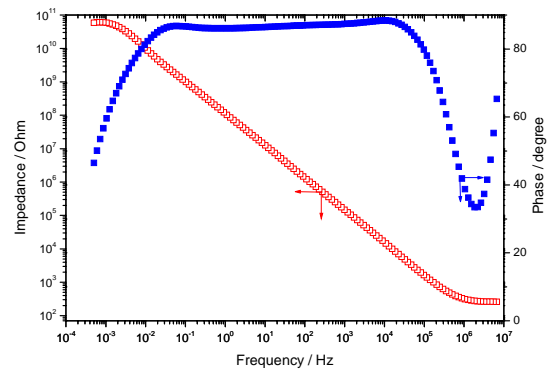
(a) Oxide thickness: $3.8\mu\text{m}$

(b) Oxide thickness: $38.8\mu\text{m}$

Figure 4.36: Bode plots of 3 day-soaked (a) thin and (b) thick oxide of Zr-0.4Nb corroded in supercritical water.



(a) Zr-1.5Nb



(b) Zr-1.0Cr-0.2Fe

Figure 4.37: EIS spectra of (a) Zr-1.5Nb and (b) Zr-1.0Cr-0.2Fe alloys corroded in supercritical water condition for 60 days.

Tensile test for the model alloys

Since the maximum doses and temperatures of supercritical water reactor are similar to that of a fast reactor, thermal stability of the alloys for the cladding tube is required. So, to select the most promising candidate alloys we have to get available data on the mechanical stability. To get data on mechanical properties on which the alloys can be considered as candidate alloys for the cladding tube for the supercritical reactor, tensile tests of the model alloys were performed both at room temperature and 500°C in accordance with ASTM E8.

The thickness of the sheet specimens for the tensile test was about 1.0 mm. The specimens were machined to be about 3.0 mm in width and 12.5 mm in the nominal gage length. The tensile tests were carried out at room temperature with the strain rate 0.005(mm/mm)/min through yield stress and 0.05(mm/mm)/min after yield stress to failure. The tensile tests at 500C had been done in 10^{-2} torr vacuum environment with the strain rate 0.05(mm/mm)/min to failure.

Figure 4.38 indicates the change of ultimate tensile strength (UTS) with the increase of Nb content. The strength of Zr-Nb alloys increase with Nb content. If the model alloys contain Nb over 1.5%, the alloys showed higher UTS than Zircaloy-4. It appears that Nb element was dissolved in the matrix to cause solid solution as well as precipitation hardening. Figure 4.39 shows the UTS and elongation of Zr-1.0X alloys. At room temperature, Zr-1.0Cu alloy has higher UTS than Zr-1.0Nb alloy and Zr-1.0Cu-0.5Mo alloy has higher UTS than Zr-1.0Cu alloy due to alloying effect on the strength. Zr-1.0Cr-0.2Fe alloy has the highest UTS among the alloys tested. At 500C, however, the strength of the alloys does not show any trend because the hardening effect of alloying element almost disappears in the high temperature. The UTS of F/M steel is 640MPa at room temperature and 425MPa at 500C. The UTS is higher than that of the Zr-based model alloys because the main element of F/M steel is Fe having BCC structure, and Cr which increases the strength in an elevated environment is added in the F/M steel. For Zr-based alloys, they have a limitation on alloying elements and their content since the alloying elements have an effect on the corrosion resistance and neutron absorption cross section of the Zr-based alloy for cladding to show lower strength than F/M steel.

On the other hand, it was difficult to find any trend of the change of elongation in the alloy system. But in general, addition of alloying element to the model alloys increased their strength and decreased their elongation. The total elongation of F/M steel are 20% at room temperature and 17.5% at 500C, whereas that of the model alloys was 30~40% at room temperature and over 60% at 500C. Thus, the model alloys has better property in ductility than in strength.

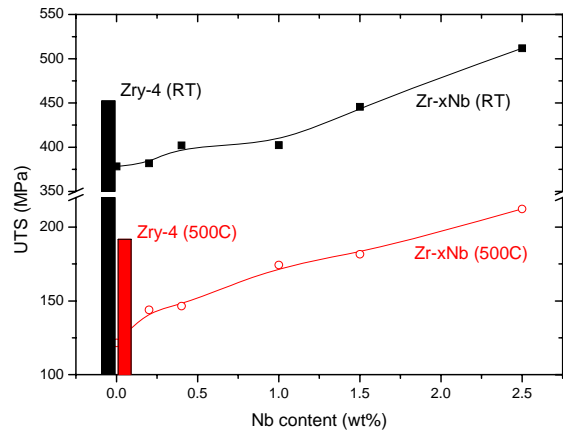


Figure 4.38: Mechanical properties of Zr-Nb alloys with the change of Nb content

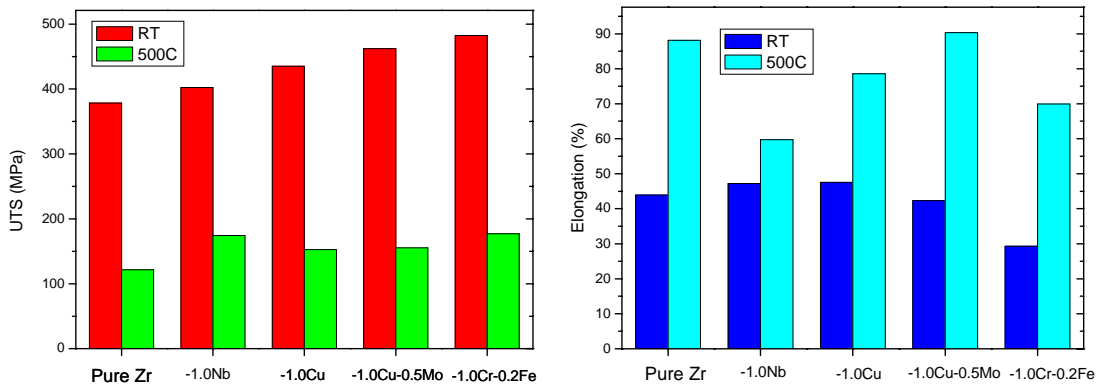


Figure 4.39: Strength and elongation of Zr-1.0X alloys

References

- [1] A. T. Motta, A. Yilmazbayhan, R. J. Comstock, J. Partezana, S. G.P., Z. Cai., and B. Lai, "Microstructure and Growth Mechanism of Oxide Layers Formed in Zr Alloys Studied with Micro Beam Synchrotron Radiation," Journal of ASTM International, vol. 2, (2005), Paper # JAI 12375.
- [2] A. Motta, A. Yilmazbayhan, M. G. d. Silva, R. J. Comstock, G. Was, J. Busby, E. Gartner, Q. Peng, Y. H. Jeong, and J. Y. Park, "Zirconium Alloys for Supercritical Water Reactor Applications: Challenges and Possibilities," Journal of Nuclear Materials, vol. submitted, (2006).
- [3] N. Petigny, P. Barberis, C. Lemaignan, C. Valot, and M. Lallemand, "In situ XRD analysis of the oxide layers formed by oxidation at 743 K on Zircaloy-4 and Zr-1NbO," Journal of Nuclear Materials, vol. 280, (2000), 318-330.
- [4] H. Li, H. M. Glavicic, and J. A. Spuznar, "A Model of Texture formation in ZrO₂ Films," Materials Science and Engineering, vol. A366, (2004), 164-174.
- [5] J. J. Kearns and C. R. Woods, J. Nucl. Mater., vol. 20, (1966), 241.
- [6] A. Yilmazbayhan, A. T. Motta, R. J. Comstock, G. P. Sabol, B. Lai, and Z. Cai, "Structure of Zirconium Alloy Oxides formed in pure water studied with Synchrotron radiation and optical microscopy: relation to corrosion rate," Journal of Nuclear Materials, vol. 324, (2004), 6-22.
- [7] A. Yilmazbayhan, A. T. Motta, H.G.Kim, Y. H. Jeong, J. Y. Park, and R. Comstock, "Characterization of oxides formed on model Zr alloys in 360 C water using synchrotron radiation," 12th International Conference on Environmental Degradation of Materials in Nuclear Power Systems -Water Reactors, Snowbird, Utah, (2005), TMS, vol., 201-210.
- [8] A. T. Motta, A. Yilmazbayhan, R. J. Comstock, B. Lai, and Z. Cai, "Using small x-ray beams to understand corrosion in nuclear fuel cladding," Proceedings of IMECE04, ASME Annual Conference, Anaheim, CA, (2004), vol., paper number 62475.
- [9] K. T. Erwin, O. Delaire, A. T. Motta, R. C. Birtcher, Y. Chu, and D. Mancini, "Observation of second-phase particles in bulk zirconium alloys using synchrotron radiation," Journal of Nuclear Materials, vol. 294, (2001), 299-304.
- [10] A. T. Motta, K. T. Erwin, O. Delaire, R. C. Birtcher, Y. Chu, J. Maser, D. C. Mancini, and B. Lai, "Synchrotron Radiation Study of Second Phase Particles and Alloying Elements in Zirconium Alloys," Zirconium in the Nuclear Industry: 13th International Symposium, Annecy, France, (2001), ASTM, vol. STP 1423, 59-78.
- [11] A. Yilmazbayhan, O. Delaire, A. T. Motta, R. C. Birtcher, J. M. Maser, and B. Lai, "Determination of the Alloying Content in the Matrix of Zr Alloys Using Synchrotron Radiation Microprobe X-Ray Fluorescence," Journal of Nuclear Materials, vol. 321, (2003), 221-232.
- [12] Z. Cai, B. Lai, W. Yun, P. Ilinski, D. Legnini, J. Maser, and W. Rodrigues, "A Hard X-Ray Scanning Microprobe for Fluorescence Imaging and Microdiffraction at the Advanced Photon Source," The Sixth International Conference for X-Ray Microscopy,, (2000), vol. AIP Proceedings 507, 472.
- [13] J.-L. Bechade, R. Brenner, P. Goudeau, and M. Gailhanou, "Influence of temperature on X-ray diffraction analysis of ZrO₂ oxide layers formed on zirconium based alloys using a synchrotron radiation," Proceedings of the 6th European Conference on

- Residual Stresses, Jul 10-12 2002, Coimbra, Portugal, (2002), Trans Tech Publications Ltd, vol. 404-407, 803-808.
- [14] R. C. Garvie, "Stabilization of the Tetragonal Structure in Zirconia Microcrystals," The Journal of Physical Chemistry, vol. 82, (1978), 218-224.
- [15] R. C. Garvie, "The Occurrence of Metastable Tetragonal Zirconia as a Crystalline Size Effect," The Journal of Physical Chemistry, vol. 69, (1965), 1238-1243.
- [16] A. Yilmazbayhan, E. Breval, A. Motta, and R. Comstock, "Transmission Electron Microscopy Examination of Oxide Layers Formed in Zr Alloys," Journal of Nuclear Materials, vol. 349, (2006), 265-281.
- [17] J. Godlewski, "How the Tetragonal Zirconia is Stabilized in the Oxide Scale that is Formed on a Zirconium Alloy Corroded at 400 C in steam," 10th Int.Symp. on Zr in the Nuclear Industry, (1994), ASTM, vol. STP 1245, 663-686.
- [18] J. Godlewski, J. P. Gros, M. Lambertin, J. F. Wadier, and H. Weidinger, "Raman Spectroscopy Study of the Tetragonal-to-Monoclinic transition in Zirconium oxide scales and determination of overall oxygen diffusion by nuclear microanalysis of ^{18}O ," 9th International Symposium on Zr in the Nuclear Industry, Kobe, Japan, (1991), ASTM, vol. STP 1132, 416-436.